PHYSICAL REVIEW B **90**, 035444 (2014)

Scattering theory of spin-orbit active adatoms on graphene

Alexandre Pachoud,[1,2] Aires Ferreira,[1,3] B. Özyilmaz,[1,2,4] and A. H. Castro Neto[1,2,5]
[1]*Graphene Research Centre and Department of Physics, National University of Singapore, 2 Science Drive 3, Singapore 117546, Singapore*
[2]*NUS Graduate School for Integrative Sciences and Engineering (NGS), National University of Singapore, Singapore 117456, Singapore*
[3]*Instituto de Física, Universidade Federal Fluminense, 24210-346 Niteroí, RJ, Brazil*
[4]*Nanocore, 4 Engineering Drive 3, National University of Singapore, Singapore 117576, Singapore*
[5]*Department of Physics, Boston University, 590 Commonwealth Avenue, Boston, Massachusetts 02215, USA*
(Received 6 March 2014; revised manuscript received 3 July 2014; published 28 July 2014)

The scattering of two-dimensional massless Dirac fermions from local spin-orbit interactions with an origin in dilute concentrations of physisorbed atomic species on graphene is theoretically investigated. The hybridization between graphene and the adatoms' orbitals lifts spin and valley degeneracies of the pristine host material, giving rise to rich spin-orbit coupling mechanisms with features determined by the exact adsorption position on the honeycomb lattice—bridge, hollow, or top position—and the adatoms' outer-shell orbital type. Effective graphene-only Hamiltonians are derived from symmetry considerations, while a microscopic tight-binding approach connects effective low-energy couplings and graphene-adatom hybridization parameters. Within the T-matrix formalism, a theory for (spin-dependent) scattering events involving graphene's charge carriers, and the spin-orbit active adatoms is developed. Spin currents associated with intravalley and intervalley scattering are found to tend to oppose each other. We establish that under certain conditions, hollow-position adatoms give rise to the spin Hall effect, through skew scattering, while top-position adatoms induce transverse charge currents via trigonal potential scattering. We also identify the critical Fermi energy range where the spin Hall effect is dramatically enhanced, and the associated transverse spin currents can be reversed.

DOI: 10.1103/PhysRevB.90.035444 PACS number(s): 72.25.−b, 72.80.Vp, 73.20.Hb, 75.30.Hx

I. INTRODUCTION

Graphene, being an atomically thin semimetal, allows a fine control over the charge-carrier density via the electric-field effect [1,2]. Therefore, its basic characteristics—such as the density of states [3], charge conductivity [4–6], and electron-phonon coupling [7,8]—are gate-tunable, making this material extremely versatile. The magnetic properties of graphene can be tailored as well [9], as placing the Fermi energy in the vicinity of (away from) an adatom energy level switches on (off) magnetic moments [10,11].

The properties of graphene can change even more drastically upon adsorption of certain atomic species; highly conducting in its pristine form, graphene can be transformed into an excellent insulator [12] or a granular metal [13] by chemisorption. Theoretical predictions point out yet another possibility: the manipulation of spin-orbit coupling (SOC) in chemically modified graphene [14–16]. Such an appealing perspective has gained renewed interest recently due to demonstrations of band-structure Rashba splitting in a graphene/Ni(111) system with intercalated gold [17] and giant local SOC enhancement in weakly hydrogenated graphene [18].

The control of SOC in gently modified graphene would open new directions in carbon-based spintronics, complementing previous proposals requiring magnetic fields [19] or magnetic ordering [20]. In particular, two-dimensional (2D) Dirac fermions in clean samples endowed with a SOC potential landscape could trigger robust spin-polarized currents through the spin Hall effect (SHE)—a phenomenon in which charge carriers with opposite spin states are asymmetrically scattered under the action of a driving electric field [21]. Given the importance of resonant scattering in 2D carbon[22,23], it is reasonable to expect that even dilute SOC-active "hot spots" would allow the observation of a sizable SHE. A recent study by some of the authors predicted that nanometer-sized metal clusters provide the required hot spots [24], capable of delivering giant spin Hall coefficients reminiscent of those in pure metals [25]. Furthermore, the experimental data reported in Ref. [18] strongly suggest that individual adatoms *per se* act as hot spots for enhanced spin-current generation, although the underlying spin-transport mechanisms remain unclear [16,18].

In the present paper, the scattering of charge carriers from physisorbed adatoms in monolayer graphene is investigated theoretically. The effective SOC generated by generic adatoms is explicitly derived—within a tight-binding and a continuum approach—and the associated single-impurity problems are solved analytically using standard techniques. Regarding the latter, our work generalizes the previous theory of resonant scattering from short-range impurities [22,23] to situations in which the effective impurity potentials possess a nontrivial spin and valley texture. Adatoms in their nonmagnetic state are shown to mediate rich SOC scattering mechanisms—due to an interplay between sublattice, spin, and valley degrees of freedom—that cannot be observed in large clusters for which intervalley scattering is inactive [24]. It is already known that sp^3 bonds formed by light adatoms induce large SOC due to graphene lattice out-of-plane deformation [14,16] with potential use in SHE [18]. Here instead we investigate the effects of heavy elements, which in a good approximation leave the lattice flat. We show that such species can, in principle, induce significant spin-orbit interactions if adsorbed in the hollow or top position, but not in the bridge position. The actual scattering mechanisms are seen to depend not only on the location of adatoms on the lattice, but also on their valence orbital type, i.e., p, d, or f. Strikingly, the competition between transverse spin currents generated by intravalley and

1098-0121/2014/90(3)/035444(17)

intervalley scattering processes is shown to favor certain types of adatoms in the establishment of SHE. Our calculations reveal that while hollow-position adatoms can induce large pure transverse spin currents and SHE, top-position adatoms produce transverse unpolarized currents via the charge Hall effect (CHE).

The paper is organized as follows. Section II provides a derivation of effective low-energy SOC Hamiltonians induced by generic atomic species physisorbed on graphene. This section generalizes the particular case of p outer-shell adatoms studied in Ref. [15] to nonmagnetic adatoms with any type of valence orbital [26–28], including the effects of intervalley scattering neglected in previous studies. In addition to the case of hollow adatoms [15], we consider also the experimentally relevant cases of top and bridge positions [12,29]. The Hamiltonians derived in this section describe dilute decorations, in which adsorbates located at random positions act as scattering centers and the low-energy physics is still dominated by graphene's π electrons. The superlattice dense limit, with adatoms occupying regularly spaced positions, endowing the band structure with SOC, has been studied in Refs. [15,16].

In Sec. III, the scattering theory for generic low-energy adatom models is established within a T-matrix approach. In particular, explicit expressions for cross sections in spin-conserving and spin-flip channels are given, and consequences for SHE and CHE are discussed. The conditions for the existence of low-energy regimes in which strong transverse spin or charge currents arise from scattering are discussed. Furthermore, we show that, for certain adatoms in hollow and top positions, the flow of transverse spin and charge currents can be reversed by tuning the Fermi energy.

Finally, the Appendix provides an alternative derivation of the effective impurity Hamiltonians—derived in Sec. II using symmetry arguments—starting from microscopic tight-binding Hamiltonians through Löwdin transformation. It also formulates conditions for the appearance of large transverse spin and charge currents as discussed in Sec. III in terms of microscopic hopping parameters.

II. EFFECTIVE ADATOM HAMILTONIANS

In previous approaches in the continuum, adatoms have essentially been modeled by a Dirac-peak potential $V\delta(\mathbf{r})$ in order to estimate the charge dc conductivity [4,23] of defective graphene, and to identify its dependence on the electronic density. Although this approach proved successful experimentally [30–32], it does not capture subtle effects that we aim to investigate, in particular the impact of adatoms on the charge carriers' spin and valley degrees of freedom. In what follows, we establish a continuum theory, within which an adatom situated at the origin adds a localized effective-potential term $\mathcal{V}\delta(\mathbf{r})$ to pristine graphene's Dirac Hamiltonian, and $\mathcal{V}$ is an 8×8 matrix that depends on the adatom's exact position in the lattice: at the center of a honeycomb hexagon (hollow position), on top of a carbon atom (top position), or in the middle of a carbon-carbon bond (bridge position). For the continuum approach to incorporate the most important symmetries associated with these particular adsorption sites, we first derive very general graphene-only tight-binding Hamiltonians, and eventually take the limit of vanishingly small lattice spacing. The results derived here form the basis for the scattering theory developed later in Sec. III.

A. Adatoms in the hollow position

We start by considering the case of a single adatom in the hollow position. As stated in the Introduction, our main goal is to develop a general description of scattering from SOC-active nonmagnetic atomic species weakly affecting carbon-carbon bonds [15,26]. Consequently, it suffices to describe the graphene-adatom system with an effective p_z-orbital tight-binding model, supplemented with a local interaction term describing the hybridization of graphene's carbon atoms with the relevant adatom (outer-shell) orbital. As we are primarily concerned with SOC, we decide to write our graphene-only Hamiltonian in terms of creation and annihilation operators of states with well-defined angular momentum, instead of the more conventional creation and annihilation operators of carbon p_z-orbital states. Since hopping integrals decrease exponentially with distance from the adatom, the relevant states of definite angular momentum can be written as a superposition of all p_z-orbital states located at the six vertices of the hexagon occupied by the adatom, as depicted in Fig. 1.

Using the numbering of carbon atoms shown in Fig. 1, and denoting the operator annihilating a p_z-orbital state of atom n by c_n, we focus on operators of the form $C=\sum_{n=1}^{6}\lambda_n c_n$. We also denote by $s_{l=x,y,z}$ the Pauli matrices acting on spin. Requiring C to have a given angular momentum, there exists an integer m such that C transforms into $e^{-is_z\pi/6}e^{-im\pi/3}C$ under in-plane rotation by $\pi/3$ around the adatom. This condition imposes that $\lambda_2=\omega^m\lambda_1,\ldots,\lambda_6=\omega^{5m}\lambda_1$, where $\omega=e^{-i\pi/3}$, i.e., the only possible operators annihilating a quasiparticle state on the hexagonal plaquette hosting the adatom, and of well-defined angular momentum around this adatom, are, up to a scalar coefficient and unitary operator acting on spin, $\Omega_m=\sum_{n=1}^{6}\omega^{m(n-1)}c_n$ for $m=0,\pm1,\pm2,3$. By construction, operators Ω_m, already encountered in Ref. [15], carry angular

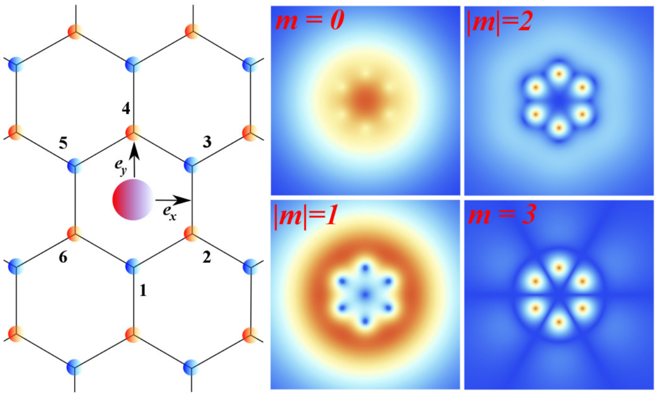

FIG. 1. (Color online) Schematic picture of an adatom (pink sphere in the left panel) in the hollow position. A-sublattice (B-sublattice) carbon atoms are represented by blue (red). Right panels show the modulus of wave functions $\psi_m(x,y)$ created by operators $\Omega_m^\dagger$, for $m=0,\pm1,\pm2,3$. Space coordinates (x,y) have the adatom as origin, and verify $(x,y)\in[-3.5,3.5]^2$ in units of $a\approx1.43$ Å. The color scale is linear and represents $|\psi_m|$, from dark blue (lowest values) to red (highest values).

momentum m, except Ω_3, which carries angular momentum 0. This can easily be seen by considering the time-reversed operator $s_y\Omega_3$, which has the same angular momentum. Since time reversal transforms angular momentum $\mathbf{L} = \mathbf{r}\times\mathbf{p}$ into its opposite, it follows that Ω_3 has angular momentum zero. We also observe that the six operators Ω_m are linearly independent, since $[\omega^{m(n-1)}]_{(m,n)}$ is a Vandermonde matrix [33] and ω is a primitive sixth root of unity. Therefore, the most general graphene-only single-electron Hamiltonian term induced by a hollow-position adatom can be written in terms of operators annihilating "hexagonal" $\Omega_m^\dagger|0\rangle$ states, that is,

$$H_{\text{hollow}} = \sum_{m=-2}^{3} \Omega_m^\dagger X_m \Omega_m + \sum_{m=-2}^{1} \Omega_m^\dagger M_m \Omega_{m+1} + \sum_{m=0,\pm1} \Omega_3^\dagger T_m \Omega_m + \text{H.c.}, \tag{1}$$

where X_m, M_m, and T_m are matrices acting on spin. These matrices connect operators Ω_i that have angular momenta differing at most by unity, by conservation of total angular momentum $J = L + S$. Conservation of J also implies that X_m and T_0 are diagonal matrices, while M_m and T_1 matrices are proportional to the spin-raising operator $s_+ = \frac{s_x+is_y}{2}$, and T_{-1} is proportional to the spin-lowering operator $s_- = \frac{s_x-is_y}{2}$. This means that under a rotation by $\pi/3$, $\Omega_m^\dagger X_m\Omega_m$ and $\Omega_m^\dagger M_m \Omega_{m+1}$ are invariant, while $\Omega_3^\dagger T_m\Omega_m$ terms are odd. The invariance of Eq. (1) under rotations by $\pi/3$ thus requires $T_{m=0,\pm1} = 0$, i.e., zero-angular-momentum states $\Omega_3^\dagger|0\rangle$ do not couple to any other hexagonal $\Omega_m^\dagger|0\rangle$ state and can be ignored. Moreover, since we consider nonmagnetic and static impurities, H_{hollow} is time-reversal invariant, which further implies that $s_y X_m^* s_y = X_{-m}$ and $s_y M_m^* s_y = M_{-m-1}^\dagger$. Finally, the invariance of H_{hollow} under reflection $x \mapsto -x$ requires $s_x X_m s_x = X_{-m}$ and $s_x M_m s_x = M_{-m-1}^\dagger$. Altogether, these conditions lead to the simplified form

$$H_{\text{hollow}} = \sum_{m=-2}^{2} \nu_m^+ \Omega_m^\dagger\Omega_m + \sum_{m=\pm1,\pm2} \nu_m^- \Omega_m^\dagger s_z \Omega_m + i\sum_{m=-2}^{1} \Lambda_m(\Omega_m^\dagger s_+ \Omega_{m+1} - \Omega_{m+1}^\dagger s_- \Omega_m), \tag{2}$$

where $\nu_m^\pm, \Lambda_m \in \mathbb{R}$ satisfying $\nu_m^\pm = \pm\nu_{-m}^\pm$ and $\Lambda_{-m-1} = -\Lambda_m$. It is important to note that Eq. (2) is general at the single-electron level, provided that interactions between the adatom and graphene's p_z orbitals are negligible outside the adatom's six nearest neighbors. The exact coupling mechanisms between hexagonal states will only affect the value of constants $\nu_m^\pm$ and Λ_m, but not the overall form of H_{hollow} given by Eq. (2). The relations between these coupling constants and the actual microscopic parameters, such as energy levels and SOCs of the adatom, are derived in the Appendix in situations where a graphene electron or hole in state $\Omega_m^\dagger|0\rangle$ undergoes spin-dependent tunneling to an adatom orbital of same angular momentum, potentially flips its spin by intra-atomic spin-orbit interaction, and tunnels back to the graphene sheet in another $\Omega_{m'\neq m}^\dagger|0\rangle$ state. In such cases, H_{hollow} describes the effect of graphene-adatom hybridization on the low-energy massless Dirac fermions.

We now derive an expression for H_{hollow} in the continuum-limit, where the carbon-carbon distance a_0 is seen as vanishingly small. In this limit, pristine graphene's Hamiltonian acquires the familiar form [34]

$$H_0 = \int \frac{d^2\mathbf{r}}{A_{\hexagon}} \Psi^\dagger(\mathbf{r})\mathcal{H}_0(\mathbf{r})\Psi(\mathbf{r}), \tag{3}$$

where $\mathcal{H}_0 = v_F(\tau_z\sigma_x p_x + \sigma_y p_y)$ and $A_{\hexagon} = 3\sqrt{3}a_0^2/2$ is the unit cell area. Here, $\tau_{l=x,y,z}$ and $\sigma_{l=x,y,z}$ are Pauli matrices acting, respectively, on valley and sublattice space [for later use, we also define $\tau_0,\sigma_0,s_0 \equiv \text{iden}(1,1)$]. In Eq. (3),

$$\Psi^\dagger(\mathbf{r}) = (\Psi_{\uparrow KA}^\dagger(\mathbf{r}), \Psi_{\uparrow KB}^\dagger(\mathbf{r}), \Psi_{\uparrow K'A}^\dagger(\mathbf{r}), \Psi_{\uparrow K'B}^\dagger(\mathbf{r}), \Psi_{\downarrow KA}^\dagger(\mathbf{r}), \Psi_{\downarrow KB}^\dagger(\mathbf{r}), \Psi_{\downarrow K'A}^\dagger(\mathbf{r}), \Psi_{\downarrow K'B}^\dagger(\mathbf{r})) \tag{4}$$

is an 8×1 creation operator whose components $\Psi_{s\tau\sigma}^\dagger(\mathbf{r})$ create a state at point $\mathbf{r}$ with spin $s = \uparrow,\downarrow \equiv 1,-1$, valley $\tau = K,K' \equiv 1,-1$, and in sublattice $\sigma = A,B \equiv 1,-1$. To account for both K and K' valleys, we write spin-s components of annihilation operators c_n as superpositions of $\Psi_{sK\sigma_n}(\mathbf{r}_n)$ and $\Psi_{sK'\sigma_n}(\mathbf{r}_n)$, where $\mathbf{r}_n$ and σ_n are the position vector and sublattice index corresponding to site n, i.e.,

$$c_{n,s} = \sum_{\tau=\pm1} e^{i\tau\overrightarrow{\Gamma K}\cdot\mathbf{r}_n}\Psi_{s\tau\sigma_n}(\mathbf{r}_n). \tag{5}$$

Here, Γ denotes graphene's first Brillouin zone center, and taking the $a_0 \to 0$ limit, the spin-s component of Ω_m becomes

$$\Omega_{m,s} = \sum_\tau \left[\gamma_{m\tau}^A \Psi_{s\tau A}(\vec{0}) + \gamma_{m\tau}^B \Psi_{s\tau B}(\vec{0})\right], \tag{6}$$

with $\gamma_{m\tau}^A = 1 + 2\cos[2\pi(m-\tau)/3]$ and $\gamma_{m\tau}^B = (-1)^m + 2\cos[\pi(m-2\tau)/3]$. Writing

$$H_{\text{hollow}} = \int \frac{d^2\mathbf{r}}{A_{\hexagon}} \Psi^\dagger(\mathbf{r})\mathcal{H}_{\text{hollow}}(\mathbf{r})\Psi(\mathbf{r}), \tag{7}$$

we obtain the following continuum-limit expression:

$$\mathcal{H}_{\text{hollow}}(\mathbf{r}) = [V_0\mathbb{I} + \Delta\tau_x\sigma_x + V_{\text{so}}s_z\tau_z\sigma_z + \Delta_{\text{so}}s_z\tau_y\sigma_y + \Lambda_R(s_x\sigma_y + s_y\tau_z\sigma_x)]A_{\hexagon}\delta(\mathbf{r}), \tag{8}$$

where $\mathbb{I}$ is the 8×8 identity matrix, $V_0 = 9(\nu_1^+ + \nu_2^+)$, $\Delta = 9(\nu_2^+ - \nu_1^+)$, $V_{\text{so}} = 9(\nu_1^- - \nu_2^-)$, $\Delta_{\text{so}} = 9(\nu_1^- + \nu_2^-)$, and $\Lambda_R = -9\Lambda_1$. Hereafter, $A_{\hexagon}$ is set to unity unless specified otherwise. We remark that Eq. (8) is only valid in the vicinity of the Dirac point, as terms of order 1 or higher in momentum k have been neglected. It nonetheless gives insight regarding possible SOC mechanisms induced by hybridization. Indeed, in addition to expected on-site potential $V_0\mathbb{I}$ [23] and Kane-Mele [35] intrinsic SOC terms $V_{\text{so}}s_z\tau_z\sigma_z$ discussed in Ref. [15], $\mathcal{H}_{\text{hollow}}$ contains a spin-independent intervalley term $\Delta\tau_x\sigma_x$ and a term $\Delta_{\text{so}}s_z\tau_y\sigma_y$ that mixes both spin and valley degrees of freedom. The presence of $\Delta\tau_x\sigma_x$ reflects the fact that atomically small impurities tend to act as "white noise" [36] in momentum space and hence make intravalley and intervalley scattering processes equiprobable. Similar to the intrinsic SOC term $V_{\text{so}}s_z\tau_z\sigma_z$, the term $\Delta_{\text{so}}s_z\tau_y\sigma_y$ is even under $\mathcal{R}_z : z \mapsto -z$ reflection. However, the former differs from the latter by its valley-connecting character, itself a direct consequence of the short-range nature of adatoms. Importantly, $\mathcal{H}_{\text{hollow}}$ also contains a term $\mathcal{H}_R = \Lambda_R(s_x\sigma_y + s_y\tau_z\sigma_x)\delta(\mathbf{r})$ originating from couplings between hexagonal states of total angular momentum $J = \pm\frac{3}{2}$, namely $\Omega^\dagger_{\pm1}s_\pm\Omega_{\pm2}$ and $\Omega^\dagger_{\pm2}s_\mp\Omega_{\pm1}$ in Eq. (2). Since p orbitals accommodate two states of angular momentum $\pm3/2$, p outer-shell adatoms can in principle mediate spin-orbit interactions between hexagonal states $\Omega^\dagger_{1,\uparrow}|0\rangle$ and $\Omega^\dagger_{2,\downarrow}|0\rangle$, thereby leading to nonzero Λ_R. This is confirmed by calculations performed with Löwdin's method, shown in the Appendix. However, Λ_R should be significantly enhanced in situations where SOC is mediated by d- or f-orbital adatoms, which host four states of angular momentum $\pm3/2$.

The symmetries of $\mathcal{H}_R$ are interesting in their own right. This term is odd under $\mathcal{R}_z$ but differs from the familiar Bychkov-Rashba Hamiltonian $\mathcal{H}_{\text{BR}} = \Lambda_{\text{so}}(s_x\sigma_y - s_y\tau_z\sigma_x)$ induced by out-of-plane electric fields [37], a possibility already predicted in Ref. [38] for inversion symmetry-breaking impurities. Similarly to the Bychkov-Rashba Hamiltonian, $\mathcal{H}_R$ is SO(2)-symmetric, as it should be for spin-orbit interactions induced by hollow-position adatoms, which preserve graphene's C_{6v} symmetry. However, we note that spinors $\psi(\mathbf{r})$ verifying $(\mathcal{H}_0 + \mathcal{H}_{\text{hollow}})\psi = E\psi$ transform under rotation by ϕ, denoted by $\mathcal{R}_\phi$, as $e^{+is_z\phi/2}e^{-i\tau_z\sigma_z\phi/2}\psi[\mathcal{R}_{-\phi}(\mathbf{r})]$. As a result, $\tau\sigma - s$ is a conserved quantity, but *not* $\tau\sigma + s$.

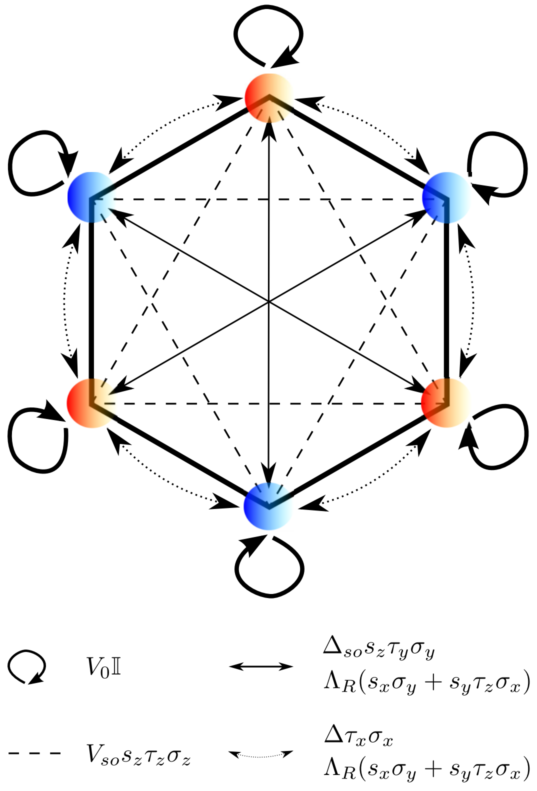

FIG. 2. (Color online) Interpretation of the effective Hamiltonian $\mathcal{H}_{\text{hollow}}$ in terms of the hopping between graphene's p_z orbitals. Given the short-range nature of the adatom-induced effective potential, all atoms around the adatom mutually interact. Intervalley terms arise from hopping between adjacent atoms. Although they were neglected in previous works [15,16], these terms play a central role in scattering from dilute random ensembles of adatoms.

Finally, let us mention that the Hamiltonian $\mathcal{H}_{\text{hollow}}$ can easily be interpreted in terms of hopping between graphene's p_z orbitals closest to the adatom, as illustrated by Fig. 2. While scalar potential $V_0\mathbb{I}$ and intrinsic SOC term $V_{\text{so}}s_z\tau_z\sigma_z$ are associated with on-site energies and hopping between second nearest neighbors, intervalley terms $\Delta\tau_x\sigma_x$ and $\Delta_{\text{so}}s_z\tau_y\sigma_y$ correspond to first- and third-nearest-neighbor hopping, respectively. In contrast with Bychkov-Rashba spin-orbit interaction $\mathcal{H}_{\text{BR}}$, the $\Lambda_R(s_x\sigma_y + s_y\tau_z\sigma_x)$ term is associated with *both* first- and third-nearest-neighbor hopping.

B. Adatoms in the top position

Another important class of adatoms are species that can be physisorbed or chemisorbed in the top position, i.e., on top of a graphene carbon atom belonging to the A or B sublattice, as depicted in Fig. 3. Such an adatom breaks graphene's C_{6v} symmetry and hence induces SOC mechanisms different from those introduced by adatoms in the hollow position; a top-position adatom has only one nearest neighbor, located directly below and numbered as 0 in Fig. 3 (as well as three second nearest neighbors labeled 1, 2, and 3 and situated at a distance of a_0 away from 0). The electronic states with definite angular momentum m formed by linear combinations of p_z orbitals at sites 1, 2, and 3 are "triangular states" annihilated by operators $\Gamma_m = \sum_{n=1}^{3}\zeta^{m(n-1)}c_n$, where $m = 0,\pm1$ and $\zeta = e^{-i2\pi/3}$. In particular, states with angular momentum ±2 are not supported. Since Γ_0, Γ_1, and Γ_{-1} are linearly independent, we can write the graphene-only impurity Hamiltonian H_{top}, describing the action of a top-position adatom, in terms of operators c_0 and $\Gamma_{0,\pm1}$ only, provided that interactions between

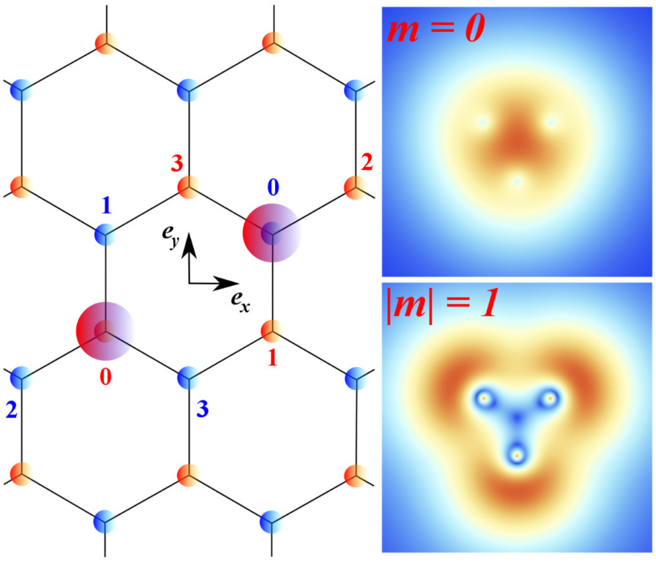

FIG. 3. (Color online) Schematic picture of adatoms (pink spheres) in the top position, on an A-sublattice (blue) and B-sublattice (red) carbon atom. Site numbering used in the main text is shown for both the A and B sublattice. Right panels show the modulus of wave functions $\phi_m(x,y)$ created around the A-sublattice adatom by operators $\Gamma^\dagger_m$, for $m = 0,\pm1$. Space coordinates (x,y) have this adatom as origin, and verify $(x,y) \in [-3.5,3.5]^2$ in units of $a \approx 1.43$ Å. The color scale is linear and represents $|\phi_m|$, from dark blue (lowest values) to red (highest values).

the adatom and more distant carbon atoms are negligible. The most general time-reversal invariant H_{top} conserving total angular momentum and preserving C_{3v}-symmetry reads

$$\begin{aligned} H_{\text{top}} = {} & V_0 c_0^\dagger c_0 + V_1 \Gamma_0^\dagger \Gamma_0 + V_2 (c_0^\dagger \Gamma_0 + \Gamma_0^\dagger c_0) \\ & + \Lambda_+ (\Gamma_1^\dagger \Gamma_1 + \Gamma_{-1}^\dagger \Gamma_{-1}) + \Lambda_- (\Gamma_1^\dagger s_z \Gamma_1 + \Gamma_{-1}^\dagger s_z \Gamma_{-1}) \\ & + i\mu (c_0^\dagger s_+ \Gamma_1 + c_0^\dagger s_- \Gamma_{-1} - \text{H.c.}) \\ & + i\tau (\Gamma_0^\dagger s_+ \Gamma_1 + \Gamma_0^\dagger s_- \Gamma_{-1} - \text{H.c.}), \end{aligned} \tag{9}$$

where $V_{0,1,2},\tau,\mu,\Lambda_\pm \in \mathbb{R}$. In the continuum limit $a_0 \to 0$, spin-s components of c_0 and Γ_m operators are $c_{0,s} = \Psi_{sKA}(\vec{0}) + \Psi_{sK'A}(\vec{0})$ and $\Gamma_{m,s} = 3(1-\delta_{m,0})\Psi_{smB}(\vec{0})$ if the adatom is on top of an A-sublattice carbon atom, and $c_{0,s} = \Psi_{sKB}(\vec{0}) + \Psi_{sK'B}(\vec{0})$ and $\Gamma_{m,s} = 3(1-\delta_{m,0})\Psi_{s,-m,A}(\vec{0})$ otherwise. In the continuum, an adatom on top of an A,B-sublattice site thus induces the following interaction:

$$\begin{aligned} \mathcal{H}_{\text{top}}^{A(B)}(\mathbf{r}) = {} & [V_0(\tau_0 + \tau_x)\pi_{A(B)} + v_0 \pi_{B(A)} \pm \lambda_{\text{so}} s_z \tau_z \pi_{B(A)} \\ & + \Lambda_{\text{so}}(s_x \tau_x \sigma_y + s_x \sigma_y + s_y \tau_z \sigma_x \pm s_y \tau_y \sigma_y)]\delta(\mathbf{r}), \end{aligned} \tag{10}$$

where $\pi_{A(B)} = (\sigma_0 \pm \sigma_z)/2$ are projectors on the $A(B)$ sublattice, $v_0 = 9\Lambda_+$, $\lambda_{\text{so}} = 9\Lambda_-$, and $\Lambda_{\text{so}} = \frac{9}{2}\mu$. The first term in Eq. (10) has already been derived for atomically sharp potentials [36]. It induces intervalley scattering and is symmetric under $x \mapsto -x$ reflection $\mathcal{R}_x$, but it breaks all rotational symmetries in the continuum theory. The latter is borne out by the local density of states maps in the vicinity of such impurities [39], exhibiting fringes perpendicular to $\overrightarrow{KK'}$ and hence to $\mathbf{e}_x$. Invariance under $\mathcal{R}_x$ is manifest, as $\mathcal{U}_x H_{\text{top}}^{A(B)} \mathcal{U}_x = H_{\text{top}}^{A(B)}$, where $\mathcal{U}_x = s_x \tau_x$ is the unitary representation of $\mathcal{R}_x$ in the continuum theory described by $\mathcal{H} = \mathcal{H}_0 + \mathcal{H}_{\text{top}}^{A(B)}$. Importantly, one also has $\mathcal{U}_y \mathcal{H}_{\text{top}}^A \mathcal{U}_y = \mathcal{H}_{\text{top}}^B$, with $\mathcal{U}_y = s_y \sigma_x$, that is, $\mathcal{H}_{\text{top}}^A$ transforms into $\mathcal{H}_{\text{top}}^B$ under $\mathcal{R}_y : y \mapsto -y$, faithfully reflecting the underlying lattice geometry. This means that top-position adatoms induce different SOC terms, depending on the host sublattice. Both close cousins of graphene's intrinsic SOC, $\mathcal{R}_z$-even spin-orbit interaction mediated by top-position adatoms on an A and B sublattice are $\lambda_{\text{so}} s_z \tau_z \pi_B \delta(\mathbf{r})$ and $-\lambda_{\text{so}} s_z \tau_z \pi_A \delta(\mathbf{r})$, respectively. The $\mathcal{R}_z$-odd component is more surprising. In addition to the valley-preserving term $\propto (s_x \sigma_y + s_y \tau_z \sigma_x)\delta(\mathbf{r})$ already encountered in Eq. (8), a new valley-mixing term $\Lambda_{\text{so}}(s_x \tau_x \sigma_y \pm s_y \tau_y \sigma_y)\delta(\mathbf{r})$ emerges, $+$ for $\mathcal{H}_{\text{top}}^A$ and $-$ for $\mathcal{H}_{\text{top}}^B$. Since in the continuum limit $\Gamma_0 = O(a_0 p)$, spin-flipping processes coupling two triangular states are quenched, in contrast with those coupling a triangular state $\Gamma_{\pm 1}^\dagger |0\rangle$ with the central orbital $c_0^\dagger |0\rangle$, whose continuum limit is a superposition of K- and K'-valley states. This explains why top-position adatoms give rise to $\mathcal{R}_z$-odd spin-orbit interactions inducing both spin-flip and intervalley scattering.

We finally note that, similar to hollow-position adatoms, the continuum limit for top adatoms can be interpreted in terms of hopping between p_z orbitals, as shown in Fig. 4. While spin-independent terms $V_0(\tau_0 + \tau_x)\pi_{A(B)}$ and $v_0 \pi_{B(A)}$ correspond to on-site energies on central site 0 and neighboring orbitals $i = 1,2,3$, respectively, the $\mathcal{R}_z$-even SOC term $\pm\lambda_{\text{so}} s_z \tau_z \pi_{B,A}$ is associated with hopping between orbitals $i \geqslant 1$. Finally, the $\mathcal{R}_z$-odd term $\Lambda_{\text{so}}(s_x \tau_x \sigma_y + s_x \sigma_y + s_y \tau_z \sigma_x \pm s_y \tau_y \sigma_y)$ arises from spin-dependent hopping between the central site 0 and its first nearest neighbors.

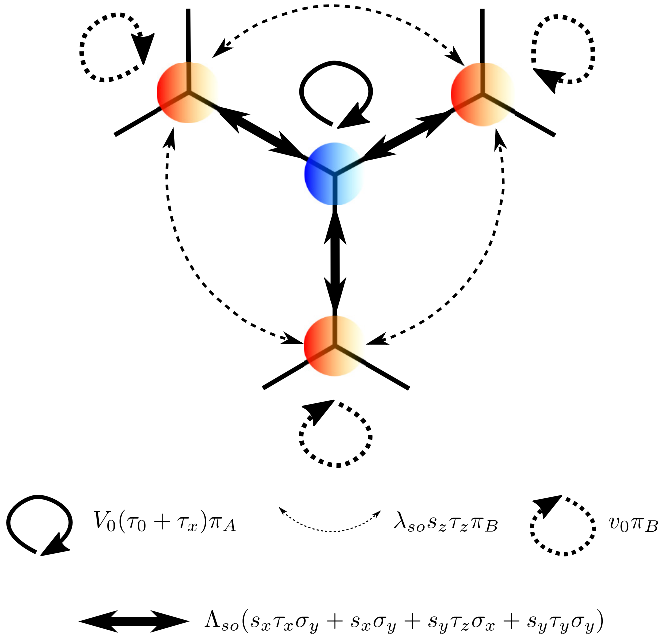

FIG. 4. (Color online) Interpretation of effective Hamiltonian $\mathcal{H}_{\text{top}}^A$ in terms of hopping between graphene's p_z orbitals.

C. Adatoms in the bridge position

We now consider the case of adatoms in the bridge position, depicted in Fig. 5. The only states of definite angular momentum m which can be formed with p_z orbitals of atoms 1 and 2 are, up to a scalar and a unitary matrix acting on spins, $(c_1^\dagger \pm c_2^\dagger)|0\rangle$. However, these states have angular momentum zero. Other possible linear combinations of angular momentum m including additional p_z orbitals would also have $m = 0$, because the only rotational symmetry

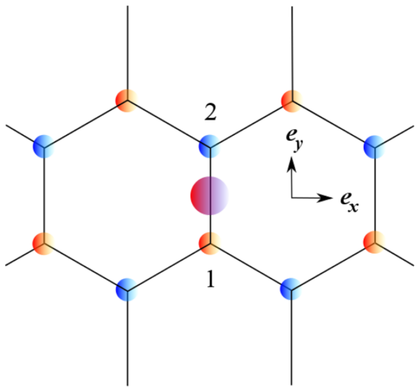

FIG. 5. (Color online) Adatom (pink sphere) in the bridge position. A- and B-sublattice carbon atoms are shown in blue and red, respectively. Relevant atoms are numbered as in the main text.

TABLE I. Comparison of effective potentials induced by spin-independent, $\mathcal{R}_z$-even, and $\mathcal{R}_z$-odd terms of impurity Hamiltonians originating from adatoms in hollow, top (on the A or B sublattice), and bridge positions. Results are valid for adatoms with generic outer-shell orbital.

Effective potential	Hollow position	Top (A or B) position	Bridge position
$\mathcal{V}_{\rm el}$	$V_0\mathbb{I} + \Delta\tau_x\sigma_x$	$V_0(\tau_0+\tau_x)\pi_{A\,(B)} + v_0\pi_{B\,(A)}$	$V_b(\tau_0+\tau_x) + \beta(\tau_0+\tau_x)\sigma_x$
$\mathcal{V}^{\rm so}_{\rm even}$	$V_{\rm so}s_z\tau_z\sigma_z + \Delta_{\rm so}s_z\tau_y\sigma_y$	$\pm\lambda_{\rm so}s_z\tau_z\pi_{B\,(A)}$	0
$\mathcal{V}^{\rm so}_{\rm odd}$	$\Lambda_R(s_x\sigma_y + s_y\tau_z\sigma_x)$	$\Lambda_{\rm so}(s_x\tau_x\sigma_y + s_x\sigma_y + s_y\tau_z\sigma_x \pm s_y\tau_y\sigma_y)$	0

preserved by the bridge configuration is the rotation by π. As a result, $\mathcal{R}_z$-odd SOC mechanisms induced by graphene-adatom hybridization is forbidden in the absence of electric-field effects. Furthermore, the impurity Hamiltonian $H_{\rm bridge}$ induced by any nonmagnetic, static bridge-position adatom must respect hermiticity, time-reversal symmetry, and $\mathcal{R}_y$. At the single electron level, and limiting ourselves to orbitals 1 and 2, these conditions constrain $H_{\rm bridge}$ to read $H_{\rm bridge} = V_b(c_1^\dagger c_1 + c_2^\dagger c_2) + \beta(c_2^\dagger c_1 + c_1^\dagger c_2)$, where $V_b,\beta \in \mathbb{R}$. Clearly, $H_{\rm bridge}$ does *not* have any SOC term, but for completeness, we derived the continuum limit of $H_{\rm bridge}$, using $c_{1,s} \to \Psi_{sKB}(\vec{0}) + \Psi_{sK'B}(\vec{0})$ and $c_{2,s} \to \Psi_{sKA}(\vec{0}) + \Psi_{sK'A}(\vec{0})$. We obtain $\mathcal{H}_{\rm bridge} = (\tau_0 + \tau_x)(V_b + \beta\sigma_x)\delta(\mathbf{r})$.

In summary, adatoms in the hollow, top, and bridge positions give rise to an interaction term $\mathcal{V}$ in the continuum-limit Hamiltonian describing graphene quasiparticles,

$$\mathcal{H}(\mathbf{r}) = v_F(\tau_z\sigma_x p_x + \sigma_y p_y) + \mathcal{V}\delta(\mathbf{r}), \tag{11}$$

where $\mathcal{V} = \mathcal{V}_{\rm el} + \mathcal{V}^{\rm so}_{\rm even} + \mathcal{V}^{\rm so}_{\rm odd}$ are, in the close vicinity of the Dirac point, momentum-independent 8×8 Hermitian matrices. Here, $\mathcal{V}_{\rm el}$ describes the spin-independent part (of pure electrostatic origin), while $\mathcal{V}^{\rm so}_{\rm even}$ and $\mathcal{V}^{\rm so}_{\rm odd}$ correspond to $\mathcal{R}_z$-even and $\mathcal{R}_z$-odd SOC contributions, respectively. Expressions for these matrices in the previously discussed cases are compared in Table I.

III. SCATTERING THEORY

A. Scattering cross-section formalism

In what follows, we consider a hollow- or top-position adatom on graphene, centered at the origin and inducing an effective potential $\mathcal{V}\delta(\mathbf{r})$. For concreteness, we take the spin-quantization axis along the z axis (i.e., out-of-plane). The results derived below can be used to obtain cross sections for arbitrary spin polarization following standard recipes; see e.g., Ref. [24]. The impurity induces elastic scattering: incoming Dirac plane waves $\phi_{\mathbf{k}}^{s,\tau}(\mathbf{r})$ of spin s, valley τ, momentum $\mathbf{k}$, and energy $E = s_E\hbar v_F k$, where $s_E = \pm 1 = {\rm sgn}(E)$, scatter to outgoing waves $\phi_{\rm out}(\mathbf{r})$, giving rise to a total wave function $\Phi(\mathbf{r}) = \phi_{\mathbf{k}}^{s,\tau}(\mathbf{r}) + \phi_{\rm out}(\mathbf{r})$ of energy E. The outgoing and incoming waves are related by the the Lippmann-Schwinger equation [40]

$$\phi_{\rm out}(\mathbf{r}) = G_0^{\pm}(\mathbf{r},E)T(E)\phi_{\mathbf{k}}^{s,\tau}(\vec{0}), \tag{12}$$

where $G_0^{\pm}(\mathbf{r},E) = \langle \mathbf{r}|(E - \mathcal{H}_0 + is_E 0^+)^{-1}|\vec{0}\rangle$ is the pristine graphene Green's function; here, is_E0^+ selects the retarded or the advanced part, corresponding to outgoing waves in electron and hole sectors, respectively. The matrix T satisfies the equation

$$T(E) = \mathcal{V}(\mathbb{I} - g(E)\mathcal{V})^{-1}. \tag{13}$$

In the above, $g(E)$ is the retarded (advanced) Green's function in the electron (hole) sector, evaluated at the origin, which is a scalar given by

$$g(E) = \frac{E}{2\pi}\ln\frac{|E|}{E_{\rm c}} - i\frac{E}{4}, \tag{14}$$

where $E_{\rm c}$ is graphene's half band-width and $\hbar v_F \equiv 1$ has been set. For the sake of simplicity, we write the T matrix and $G_0^{\pm}(\mathbf{r},E)$ in the following basis of states:

$$\{|\uparrow KA\rangle, |\uparrow KB\rangle, |\uparrow K'B\rangle, |\uparrow K'A\rangle, \\ |\downarrow KA\rangle, |\downarrow KB\rangle, |\downarrow K'B\rangle, |\downarrow K'A\rangle\}, \tag{15}$$

where the Green's function takes the simple asymptotic form, as $r \to +\infty$ [23],

$$G_0^{\pm}(\mathbf{r},E) = -\sqrt{\frac{is_E k}{8\pi}}\frac{e^{ikr}}{\sqrt{r}}e^{i\tau_z\overrightarrow{\Gamma K}\cdot\mathbf{r}}(\mathbb{I} + s_0\tau_z\sigma_\theta), \tag{16}$$

with $\sigma_\theta = \cos\theta\sigma_x + \sin\theta\sigma_y$ and $\theta = \angle(\mathbf{e}_x,\mathbf{r})$. In Eq. (16), the diagonal matrix $e^{i\tau_z\overrightarrow{\Gamma K}\cdot\mathbf{r}}$ encodes the phase difference between waves at K and K' points. In the basis defined by Eq. (15), we write T in block form:

$$T = \begin{pmatrix} T_{\uparrow K,\uparrow K} & T_{\uparrow K',\uparrow K} & T_{\downarrow K,\uparrow K} & T_{\downarrow K',\uparrow K} \\ T_{\uparrow K,\uparrow K'} & T_{\uparrow K',\uparrow K'} & T_{\downarrow K,\uparrow K'} & T_{\downarrow K',\uparrow K'} \\ T_{\uparrow K,\downarrow K} & T_{\uparrow K',\downarrow K} & T_{\downarrow K,\downarrow K} & T_{\downarrow K',\downarrow K} \\ T_{\uparrow K,\downarrow K'} & T_{\uparrow K',\downarrow K'} & T_{\downarrow K,\downarrow K'} & T_{\downarrow K',\downarrow K'} \end{pmatrix}, \tag{17}$$

and we denote, for valleys τ,τ' and spins s,s',

$$T_{s\tau,s'\tau'} = \begin{pmatrix} T^{11}_{s\tau,s'\tau'} & T^{12}_{s\tau,s'\tau'} \\ T^{21}_{s\tau,s'\tau'} & T^{22}_{s\tau,s'\tau'} \end{pmatrix}. \tag{18}$$

The outgoing wave reads, away from the impurity,

$$\phi_{\rm out}(\mathbf{r}) = -\sqrt{\frac{is_E k}{8\pi}}\frac{e^{ikr}}{\sqrt{r}}e^{i\tau_z\overrightarrow{\Gamma K}\cdot\mathbf{r}}\sum_{s',\tau'} c_{s\tau,s'\tau'}(\theta)u_{k\mathbf{e}_\mathbf{r}}^{s',\tau'}(\theta), \tag{19}$$

where $\mathbf{e}_\mathbf{r} = \mathbf{r}/r$, $u_{k\mathbf{e}_\mathbf{r}}^{s',\tau'}(\theta) = 2^{-1/2}|s'\rangle \otimes |\tau'\rangle \otimes (1, s_E\tau' e^{i\theta})^{\rm t}$ in basis (15), and

$$c_{s\tau,s'\tau'}(\theta) = T^{11}_{s\tau,s'\tau'} + \tau T^{12}_{s\tau,s'\tau'} + \tau' e^{-i\theta}\left(T^{21}_{s\tau,s'\tau'} + \tau T^{22}_{s\tau,s'\tau'}\right). \tag{20}$$

Accounting for both spin and valley degrees of freedom, the probability density current associated with the outgoing wave reads

$$\mathcal{J}_r = v_F\phi_{\rm out}^\dagger s_0\tau_z\sigma_\theta\phi_{\rm out} = \frac{k}{8\pi r}v_F\sum_{s',\tau'}|c_{s\tau,s'\tau'}(\theta)|^2. \tag{21}$$

The current associated with scattering of an incoming Dirac fermion of spin s and valley τ is thus the sum of currents $\mathcal{J}_{s\tau,s'\tau'} = \frac{k}{8\pi r} v_F |c_{s\tau,s'\tau'}(\theta)|^2 \mathbf{e_r}$ arising from all possible $s\tau \to s'\tau'$ transitions, and corresponding differential cross sections $\sigma_{s\tau,s'\tau'}(\theta)$ are

$$\sigma_{s\tau,s'\tau'}(\theta) = \frac{k}{8\pi} |c_{s\tau,s'\tau'}(\theta)|^2. \tag{22}$$

An asymptotic formula for $\sigma_{s\tau,s'\tau'}(\theta)$ can easily be derived from Eq. (20):

$$\sigma_{s\tau,s'\tau'}(\theta) = \frac{k}{8\pi} \left[\mathcal{C}^2_{s\tau,s'\tau'} + \mathcal{M}_{s\tau,s'\tau'} \cos(\theta + \varphi_{s\tau,s'\tau'})\right], \tag{23}$$

where

$$\mathcal{C}^2_{s\tau,s'\tau'} = \left|T^{11}_{s\tau,s'\tau'} + \tau T^{12}_{s\tau,s'\tau'}\right|^2 + \left|T^{21}_{s\tau,s'\tau'} + \tau T^{22}_{s\tau,s'\tau'}\right|^2, \tag{24}$$

$$\mathcal{M}_{s\tau,s'\tau'} = 2\tau' \left|T^{11}_{s\tau,s'\tau'} + \tau T^{12}_{s\tau,s'\tau'}\right| \left|T^{21}_{s\tau,s'\tau'} + \tau T^{22}_{s\tau,s'\tau'}\right|, \tag{25}$$

and

$$\varphi_{s\tau,s'\tau'} = \arg\left(T^{11}_{s\tau,s'\tau'} + \tau T^{12}_{s\tau,s'\tau'}\right) - \arg\left(T^{21}_{s\tau,s'\tau'} + \tau T^{22}_{s\tau,s'\tau'}\right). \tag{26}$$

It is important to note that $\sigma_{s\tau,s'\tau'}(\theta)$ generally has a phase $\varphi_{s\tau,s'\tau'}$ [see Eq. (23)], which can give rise to skew-scattering and thus SHE, provided $\varphi_{s\tau,s'\tau'} \neq 0$ and $\mathcal{M}_{s\tau,s'\tau'} \neq 0$. Establishing conditions under which skew scattering is significant is the object of subsequent paragraphs. This study can be conveniently carried out by comparing the integrated skew cross sections,

$$\Sigma^{\perp}_{s\tau,s'\tau'} = \int_0^{2\pi} d\theta \sin\theta \sigma_{s\tau,s'\tau'}(\theta), \tag{27}$$

which measure the skewness of $s\tau \to s'\tau'$ scattering mechanisms, to the integrated transport cross sections,

$$\Sigma^{\parallel}_{s\tau,s'\tau'} = \int_0^{2\pi} d\theta (1 - \cos\theta) \sigma_{s\tau,s'\tau'}(\theta). \tag{28}$$

From a semiclassical viewpoint, these integrated cross sections relate to the microscopic currents according to

$$J^{\perp}_{s\tau,s'\tau'} = s_E \int_0^{2\pi} \mathcal{J}_{s\tau,s'\tau'} \cdot \mathbf{e}_y r\, d\theta = s_E v_F \Sigma^{\perp}_{s\tau,s'\tau'} \tag{29}$$

and

$$J^{\parallel}_{s\tau,s'\tau'} = s_E \int_0^{2\pi} \mathcal{J}_{s\tau,s'\tau'} \cdot (\mathbf{e_r} - \mathbf{e}_x) r\, d\theta = s_E v_F \Sigma^{\parallel}_{s\tau,s'\tau'}, \tag{30}$$

associated with $s\tau \to s'\tau'$ processes. The knowledge of *microscopic* currents (29) and (30), describing charge scattering with *a single impurity*, gives direct access to the steady-state charge and spin *macroscopic*currents for a random ensemble of adatoms via the standard Boltzmann transport formalism [24,41].

B. Scattering with hollow-position adatoms

We now focus on scattering mechanisms induced by an adatom in the hollow position. Making use of Table I, the calculated T matrix in the basis given by Eq. (15) reads

$$T_{\text{hollow}} = \begin{pmatrix} T^{\uparrow\uparrow}_{\text{hollow}} & T^{\downarrow\uparrow}_{\text{hollow}} \\ T^{\uparrow\downarrow}_{\text{hollow}} & T^{\downarrow\downarrow}_{\text{hollow}} \end{pmatrix}, \tag{31}$$

with 4×4 blocks,

$$T^{ss}_{\text{hollow}} = \begin{pmatrix} \alpha_s & 0 & \gamma_s & 0 \\ 0 & \beta_s & 0 & \delta_s \\ \gamma_s & 0 & \alpha_s & 0 \\ 0 & \delta_s & 0 & \beta_s \end{pmatrix}, \tag{32}$$

where $s = \uparrow,\downarrow$ and

$$T^{\uparrow\downarrow}_{\text{hollow}} = -[T^{\downarrow\uparrow}_{\text{hollow}}]^{\text{t}} = \begin{pmatrix} 0 & 0 & 0 & 0 \\ \tau_{\text{f}} & 0 & 0 & 0 \\ 0 & 0 & 0 & 0 \\ 0 & 0 & -\tau_{\text{f}} & 0 \end{pmatrix}. \tag{33}$$

Matrix elements appearing in Eqs. (32) and (33) verify

$$\tau_{\text{f}} = \frac{2i\Lambda_R}{d}, \tag{34}$$

$$\alpha_{\uparrow(\downarrow)} = \beta_{\downarrow(\uparrow)} = \frac{\chi_{\pm} - p_{\pm} g}{d_{\pm}}, \tag{35}$$

$$\gamma_{\uparrow(\downarrow)} = \delta_{\downarrow(\uparrow)} = \frac{\Delta \mp \Delta_{\text{so}}}{d_{\pm}}, \tag{36}$$

where we have set $\chi_\varsigma = V_0 + \varsigma V_{\text{so}}$ and $p_\varsigma = (V_0 + \varsigma V_{\text{so}})^2 - (\Delta - \varsigma \Delta_{\text{so}})^2 - 2(1+\varsigma)\Lambda_R^2$, with $\varsigma = \pm 1$. We also defined

$$d_\varsigma = 1 - 2g\chi_\varsigma + p_\varsigma g^2. \tag{37}$$

Strikingly, the T-matrix elements for intervalley scattering events involving spin-flip are null. However, intravalley spin-flips, spin-preserving intervalley scattering, and pure momentum scattering events are allowed, and we shall describe them in more detail in what follows.

Using Eqs. (20) and (22), we found that differential cross sections $\sigma_{\uparrow K,\downarrow K}(\theta)$, $\sigma_{\uparrow K',\downarrow K'}(\theta)$, $\sigma_{\downarrow K,\uparrow K}(\theta)$, and $\sigma_{\downarrow K',\uparrow K'}(\theta)$ are equal and isotropic, leading to

$$\Sigma^{\parallel}_{s\tau,-s\tau} = \frac{k|\tau_{\text{f}}|^2}{4}, \tag{38}$$

and null skew cross sections,

$$\Sigma^{\perp}_{s\tau,-s\tau} = 0, \tag{39}$$

that is, spin-flip does not give rise to transverse spin currents. We remark that a similar result has been recently derived for the particular case of SO(2)-symmetric intravalley potentials [24], which, in the present context, correspond to setting $\Delta, \Delta_{\text{so}} = 0$ in Eq. (8).

We now move gears to elastic (spin-preserving) scattering. In particular, intervalley scattering cross sections are characterized, for $\tau \neq \tau'$, by

$$\mathcal{M}_{s\tau,s\tau'} = \tau' \mathcal{M}_{\text{inter}}, \tag{40}$$

$$\varphi_{s\tau,s\tau'} = s\Theta_{\text{inter}} - (1-\tau)\frac{\pi}{2}, \tag{41}$$

with

$$\mathcal{M}_{\rm inter} = 2\prod_{\varsigma=\pm1}\frac{\Delta+\varsigma\Delta_{\rm so}}{|d_\varsigma|}, \tag{42}$$

$$\Theta_{\rm inter} = -\sum_{\varsigma=\pm1}\varsigma\left[\arctan\left(\frac{{\rm Im}\, d_\varsigma}{{\rm Re}\, d_\varsigma}\right)+\pi H(-{\rm Re}\, d_\varsigma)\right], \tag{43}$$

and $H(.)$ is the Heaviside step function. Generally, both $\mathcal{M}_{\rm inter}\neq 0$ and $\Theta_{\rm inter}\neq 0$ and hence intervalley scattering induced by a hollow-position adatom is skewed. The case of spin-preserving intravalley scattering is similar:

$$\mathcal{M}_{s\tau,s\tau} = \tau\mathcal{M}_{\rm intra}, \tag{44}$$

$$\varphi_{s\tau,s\tau} = s\Theta_{\rm intra} - (1-\tau)\frac{\pi}{2}, \tag{45}$$

with

$$\mathcal{M}_{\rm intra} = 2\prod_{\varsigma=\pm1}\frac{|\chi_\varsigma - p_\varsigma g|}{|d_\varsigma|}, \tag{46}$$

and

$$\Theta_{\rm intra}-\Theta_{\rm inter} = \sum_{\varsigma=\pm1}\varsigma\left[\arctan\left(\frac{{\rm Im}\, g}{{\rm Re}\, g - \frac{\chi_\varsigma}{p_\varsigma}}\right)+\pi H\left({\rm Re}\, g - \frac{\chi_\varsigma}{p_\varsigma}\right)\right]. \tag{47}$$

These results trivially lead to a zero transverse charge microcurrent,

$$J_C^\perp \equiv \sum_{s,\tau,\tau'} J^\perp_{s\tau,s\tau'} = 0, \tag{48}$$

but to a generally nonzero transverse spin microcurrent,

$$J_S^\perp \equiv \sum_{s,\tau,\tau'} sJ^\perp_{s\tau,s\tau'} = \frac{ks_E v_F}{2}\mathcal{M}_{\rm inter}(\sin\Theta_{\rm inter} - \mathcal{F}\sin\Theta_{\rm intra}), \tag{49}$$

where

$$\mathcal{F} = \frac{\mathcal{M}_{\rm intra}}{\mathcal{M}_{\rm inter}}. \tag{50}$$

The key parameters controlling the magnitude of the transverse spin-probability current $J_S^\perp$ are thus the phase difference $\vartheta = \Theta_{\rm intra} - \Theta_{\rm inter}$ and the $\mathcal{F}$ factor. They depend on the hopping energies characterizing the graphene-adatom hybridization, and are thus expected to depend strongly on the valence orbital type. Since s-orbital adatoms lack $J = \pm 3/2, \pm 5/2$ total angular momentum states, necessary to couple hexagonal states of angular momentum $m = \pm 2$, they induce zero $\nu_2^\pm, \Lambda_R$ [cf. Eq. (2)], directly leading to $p_\pm = 0$. Consequently, $\vartheta = 0$, $\mathcal{F} = 1$, and thus $J_S^\perp = 0$ for s-orbital adatoms. Interestingly, p-orbital adatoms are a limiting case: they host exactly two orbital states $J = \pm 3/2$ and no $J = \pm 5/2$ states. Therefore, $\Omega^\dagger_{\pm 2}|0\rangle \to \Omega^\dagger_{\mp 2}|0\rangle$ transitions require double spin-flips, leading to small $\nu_2^\pm \propto w_2^2$ couplings, where w_2 is the hopping energy between graphene's $\Omega^\dagger_{\pm 2,\downarrow/\uparrow}|0\rangle$ state and the adatom's p orbital with angular momentum ± 1 and spin-$\uparrow,\downarrow$; see the Appendix. Generally, p-orbital adatoms are thus expected to yield negligible ϑ, $\mathcal{F} \approx 1$, and hence small $J_S^\perp$. The cases of d- and f-orbital adatoms are noticeably different as they offer spin-preserving channels for $\Omega^\dagger_{\pm 2}|0\rangle \to \Omega^\dagger_{\mp 2}|0\rangle$ transitions, generally leading to appreciable $\nu_2^\pm$ couplings. In the low-energy limit $|g| \ll \chi_\pm/p_\pm$, the $\mathcal{F}$ factor reads

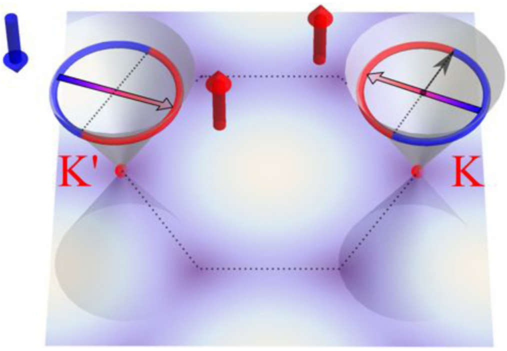

FIG. 6. (Color online) Schematic representation of skew-scattering induced by adatoms in the hollow position. The black arrow represents the momentum $\mathbf{k}_{\rm in}$ of an incoming quasiparticle in the K valley. Blue (red) half-circles correspond to the region of the Fermi line where the outgoing momentum $\mathbf{k}_{\rm out}$ is most likely to be after a scattering event, if the incoming charge carrier has spin down (spin up). Resulting pure spin currents are depicted as blue and red planar arrows. Spin currents in K and K' valleys associated with intra- and intervalley scattering tend to oppose each other.

$$\mathcal{F} \approx \left(\frac{\nu_1^+ + \nu_2^+}{\nu_1^+ - \nu_2^+}\right)^2 \neq 1, \tag{51}$$

where couplings corresponding to spin-dependent processes are neglected. Clearly, this opens up the possibility of having large $J_S^\perp$ provided $\Theta_{\rm inter}$ and/or ϑ are finite (nonzero), leading to SHE [21,42]. ϑ vanishes in the vicinity of the Dirac point, reflecting the fact that intra- and intervalley scattering mechanisms tend to yield transverse spin currents of opposite signs, as depicted in Fig. 6. However, ϑ can become significant under certain conditions. A natural question is thus whether ϑ can become large close to the Dirac point for some physically meaningful values of $p_\pm$ and $\chi_\pm$. Typically, the function ϑ peaks when ${\rm Re}\, g$ lies between $x_+ = \frac{\chi_+}{p_+}$ and $x_- = \frac{\chi_-}{p_-}$. Conditions ${\rm Re}\, g = x_\pm$ are fulfilled for Fermi levels $E_{X=x_\pm}$ verifying

$$\frac{E_X}{E_c}\ln\left|\frac{E_X}{E_c}\right| = \frac{2\pi E_{\hexagon}^2 X}{E_c}, \tag{52}$$

where constants $\hbar v_F$ and $A_{\hexagon}$ have been restored, and $E_{\hexagon} = \hbar v_F/\sqrt{A_{\hexagon}}$. Peak values of ϑ are thus attained close to the Dirac point provided that $2\pi E_{\hexagon}^2|X| \ll E_c$, in which case we find

$$\frac{E_X}{E_c} = \mathcal{L}\left(\frac{2\pi E_{\hexagon}^2 X}{E_c}\right). \tag{53}$$

Here, $\mathcal{L}$ is a function defined by means of the lower branch of the Lambert W function, $\mathcal{W}_{-1}$:

$$\mathcal{L}(y) = \frac{y}{\mathcal{W}_{-1}(-|y|)} \approx \frac{y}{\ln|y|}\left(1 + \frac{\ln|\ln|y||}{\ln|y|} + \frac{\ln^2|\ln|y||}{\ln^2|y|} - \frac{\ln|\ln|y||}{\ln^2|y|}\right). \tag{54}$$

We now determine under which conditions $2\pi E_{\hexagon}^2 |X| \ll E_c$ is verified. Parameters $p_\pm$ and $\chi_\pm$ can be expressed in terms of the adatom's energy levels as well as tight-binding parameters connecting hexagonal states to the adatom's valence orbital. If the Fermi energy lies far away from the adatom's valence orbital energy levels,

$$\chi_\pm \approx -9\left(\frac{\Upsilon_1^2}{E_{1\pm 1/2}^{+}} + \frac{\Upsilon_2^2}{E_{2\mp 1/2}^{-}}\right), \tag{55}$$

$$p_\pm \approx 324 \frac{\Upsilon_1^2 \Upsilon_2^2}{E_{1\pm 1/2}^{-} E_{2\mp 1/2}^{+}}, \tag{56}$$

where $E_J^\pm$ are energy levels that valence orbitals would have in the absence of intra-atomic spin-flip, $\Upsilon_m = u_m + v_m$, and u_m and v_m are hopping integrals connecting hexagonal states and the adatom's orbitals of the same angular momentum m; see Eq. (A12) and text therein for definitions of the hopping integrals. We thus have

$$\frac{2\pi E_{\hexagon}^2 x_\pm}{E_c} \approx -\frac{\pi E_{\hexagon}^2}{18 E_c}\left(\frac{E_{1\pm 1/2}^{+}}{\Upsilon_1^2} + \frac{E_{2\mp 1/2}^{-}}{\Upsilon_2^2}\right), \tag{57}$$

which are small provided $E_c \Upsilon_{1,2}^2 / E_{\hexagon}^2$ are significantly larger than the adatom's valence orbital energy levels.

In addition, Θ_{inter} exhibits resonances of its own, which typically occur in energy windows where the real part of $d_\pm$ is small. The real part of $d_\pm$ vanishes close to the Dirac point at energies $E_{D=d_\pm}$, which relate to $X = x_\pm$ and $C = c_\pm = \frac{p_\pm}{\chi_\pm^2}$ according to

$$\frac{E_D}{E_c} \approx \mathcal{L}\left(\frac{2\pi E_{\hexagon}^2 X}{E_c}\left[1 - \sqrt{1-C}\right]\right). \tag{58}$$

The function Θ_{inter} exhibits resonances close to the Dirac point provided that $2\pi E_{\hexagon}^2 |X| \ll E_c$ or $C \ll 1$. The former condition is valid whenever both $E_c \Upsilon_1 / E_{\hexagon}^2$ and $E_c \Upsilon_2 / E_{\hexagon}^2$ are large compared to adatom energy levels, whereas the latter condition is fulfilled if $\Upsilon_1 \gg \Upsilon_2$ or $\Upsilon_2 \gg \Upsilon_1$. More precisely, $c_\pm \propto (\Upsilon_2/\Upsilon_1)^2$ whenever $\Upsilon_1 \gg \Upsilon_2$ and $c_\pm \propto (\Upsilon_1/\Upsilon_2)^2$ in the opposite limit.

Figure 7(a) shows $J_S^\perp$ as a fraction of the charge current,

$$J_C^\parallel = s_E v_F \sum_{s,\tau,s',\tau'} \Sigma_{s\tau,s'\tau'}^{\parallel}, \tag{59}$$

against Fermi energy E_F, for realistic values of hopping integrals and atomic energy levels. While the adatom energy levels are kept fixed, $J_S^\perp / J_C^\parallel$ is plotted for different pairs of couplings (Υ_1, Υ_2), corresponding to points A, B, C, and D shown in Fig. 7(b). Figure 7(a) illustrates the strong dependence of $J_S^\perp / J_C^\parallel$ on couplings between the adatom valence orbitals and graphene hexagonal states. At point A, the transverse spin microcurrent is negligible compared to $J_C^\parallel$, whereas points B and C yield transverse spin currents as large as ∼20% of the total outgoing current at resonance. In situation D, $J_S^\perp / J_C^\parallel$ exhibits giant peak values of up to 0.4 in magnitude. Figure 7(b) connects the existence of peaks in $J_S^\perp / J_C^\parallel$ for particular (Υ_1, Υ_2) points to previously discussed resonant energies $E_{x_\pm, d_\pm}$. It highlights that $E_{x_\pm, d_\pm}$ and the resulting peaks in transverse spin currents exist at low energy for sufficiently large $|\Upsilon_1|$ or $|\Upsilon_2|$. However, the peak values of $J_S^\perp / J_C^\parallel$ only become significant when both $|\Upsilon_1|$ and $|\Upsilon_2|$ exceed $\sim E_{\hexagon} (E_J^\pm / E_c)^{1/2}$.

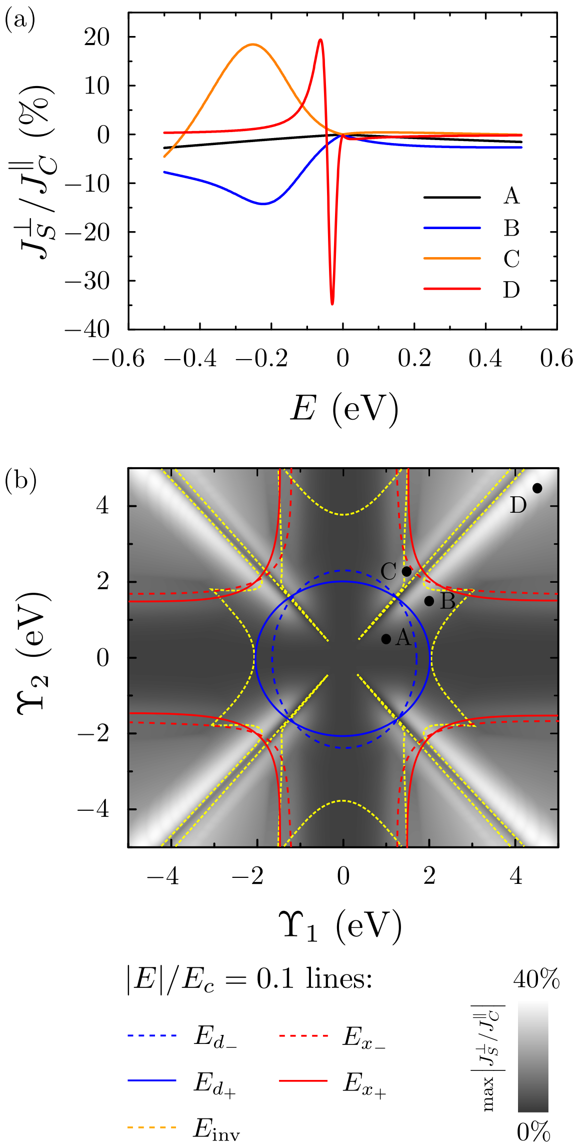

FIG. 7. (Color online) Resonant features of spin transverse currents generated by hollow-position physisorbed adatoms on graphene. (a) $J_S^\perp / J_C^\parallel$ (in %) against Fermi energy (in eV), for adatoms with $E_{1/2}^\pm = -1$ eV, $E_{3/2}^\pm = -1.5$ eV, and $E_{5/2}^\pm = -2$ eV and different (Υ_1, Υ_2), corresponding to points A, B, C, and D shown in the lower panel. (b) Maximum of $|J_S^\perp / J_C^\parallel|$ for $|E_F| \leqslant 0.5$ eV, against Υ_1 and Υ_2. $|E|/E_c = 0.1$ lines are shown for $E = E_{x_\pm, d_\pm}, E_{\mathrm{inv}}$. Each line partitions the (Υ_1, Υ_2) space into two parts: a region containing the origin $\Upsilon_1 = \Upsilon_2 = 0$, characterized by high-energy resonances, $|E|/E_c > 0.1$, and a region away from the origin, characterized by low-energy resonances, $|E|/E_c < 0.1$.

While transverse spin currents, arising from skew-scattering of graphene Dirac fermions with a hollow-position adatom, can exhibit large resonances, Eq. (49) suggests that $J_S^\perp$ possesses another interesting property. Since $J_S^\perp$ results from competing transverse spin currents originating from intra- and intervalley scattering, one expects $J_S^\perp$ to change sign for particular Fermi energies, such that

$$\tan \Theta_{\text{inter}} = \frac{\mathcal{F} \sin \vartheta}{1 - \mathcal{F} \cos \vartheta}. \tag{60}$$

The existence of such levels close to the Dirac point would open up interesting technological prospects, as a field effect would allow to reverse spin-current flows. Intriguingly, Eq. (60) admits low-energy solutions for sufficiently large $|\Upsilon_1|$ or $|\Upsilon_2|$. For the sake of clarity, points (Υ_1, Υ_2) such that the solution E_{inv} of minimum magnitude is equal to a tenth of graphene half-bandwidth are shown in Fig. 7(b) as a yellow dashed line. Energies E_{inv} closer to the Dirac point are obtained away from the origin, beyond the yellow curve. This is illustrated by point D, whose corresponding $J_S^\perp / J_C^\parallel$ against E_F curve exhibits a sharp inversion in transverse spin-current flow around $E_F \approx 50$ meV; see Fig. 7(a).

Finally, let us highlight further the specificities of the above-discussed spin currents. Although spin Hall related phenomena of intrinsic [43] and extrinsic [18] types have already been observed in graphene, they differ drastically from SHE discussed in our work. While in Ref. [43] SHE necessitates a strong magnetic field and relies on Zeeman splitting at the Dirac point [19], correlating spin ↑,↓ and charge $\mp e$, the SHE observed in Ref. [18] is induced by the deformation of a graphene lattice due to the presence of sp^3 bonds [14]. Our theory describes SHE arising from hybridization of graphene with adatoms in the hollow position, and predicts the appearance of large spin currents around resonant energies $E_{x_\pm}$ and $E_{d_\pm}$ for d- or f-orbital adatoms. The nature of these resonances is graphene-specific. Scattering events with δ impurities generally lead to outgoing waves that are linear combinations of Dirac spinors. The corresponding coefficients are of the form $\varrho_1 + \varrho_2 e^{-i\theta}$ as shown by Eq. (20). For scalar potentials, $\varrho_1 = \varrho_2$, leading to the well-known absence of backscattering [22]. However, for "tensor potentials," such as the Kane-Mele term $V_{\text{so}} s_z \tau_z \sigma_z \delta(\mathbf{r})$, the T matrix is sublattice-dependent, and ϱ_1 and ϱ_2 can thus acquire a phase difference, which gives rise to gate-tunable Θ_{intra} and Θ_{inter} [through $g(E)$], enabling the discussed resonances. The SHE arising from hollow-position adatoms on graphene is thus significantly different from extrinsic SHE phenomena typically studied in parabolic-band 2D electron gases, and the above-discussed resonances are unrelated to previously observed enhancement of skew-scattering due to the orbital-dependent Kondo effect [44] or a large SOC energy band [45]. Our calculations show that the efficiency of isolated adatoms to generate transverse spin currents, i.e., $J_S^\perp / J_C^\parallel = O(0.1)$, is comparable to that recently predicted for large SOC-active clusters [24]. Last but not least, an interesting feature of the resonant regime illustrated by Fig. 7 is the possibility to change the sign of $J_S^\perp$ upon tuning the Fermi level around specific "inversion energies" E_{inv}. A direct consequence is the ability to convert a charge current into a large transverse spin current in a certain energy range, and to reverse its flow by tuning the gate voltage around critical values, which could find applications in spin-based logic devices.

C. Scattering with top-position adatoms

We now deal with the scattering mechanisms induced by an adatom in the top position. We start with adatoms on top of an A-sublattice carbon atom. Using Table I, the corresponding T matrix in basis (15) reads

$$T_{\text{top},A} = \begin{pmatrix} T_{\text{top},A}^{\uparrow\uparrow} & T_{\text{top},A}^{\downarrow\uparrow} \\ T_{\text{top},A}^{\uparrow\downarrow} & T_{\text{top},A}^{\downarrow\downarrow} \end{pmatrix}, \tag{61}$$

with 4×4 blocks:

$$T_{\text{top},A}^{ss} = \begin{pmatrix} a & 0 & 0 & a \\ 0 & b_s & 0 & 0 \\ 0 & 0 & b'_s & 0 \\ a & 0 & 0 & a \end{pmatrix}, \tag{62}$$

where $s = \uparrow,\downarrow$ and

$$T_{\text{top},A}^{\uparrow\downarrow} = -[T_{\text{top},A}^{\downarrow\uparrow}]^{\text{t}} = \begin{pmatrix} 0 & 0 & -t & 0 \\ t & 0 & 0 & t \\ 0 & 0 & 0 & 0 \\ 0 & 0 & -t & 0 \end{pmatrix}. \tag{63}$$

The T-matrix elements in Eqs. (62) and (63) verify the following identities:

$$t = \frac{2i\Lambda_{\text{so}}}{1 - Ug + 2wg^2}, \tag{64}$$

$$a = \frac{V_0 - wg}{1 - Ug + 2wg^2}, \tag{65}$$

$$b_\uparrow = b'_\downarrow = \frac{v_0 + \lambda_{\text{so}}}{1 - g(v_0 + \lambda_{\text{so}})}, \tag{66}$$

$$b_\downarrow = b'_\uparrow = \frac{v_0 - \lambda_{\text{so}} - 2wg}{1 - Ug + 2wg^2}, \tag{67}$$

where we set $U = 2V_0 + v_0 - \lambda_{\text{so}}$ and $w = (v_0 - \lambda_{\text{so}})V_0 - 4\Lambda_{\text{so}}^2$. The T matrix for a B-sublattice adatom is easily obtained from $T_{\text{top},A}$ by reflection $\mathcal{R}_y$, i.e.,

$$T_{\text{top},B} = \mathcal{U}_y T_{\text{top},A} \mathcal{U}_y. \tag{68}$$

Matrix elements $t_{s\tau,s'\tau'}^{\sigma,\sigma'}$ and $\tilde{t}_{s\tau,s'\tau'}^{\sigma,\sigma'}$ of $T_{\text{top},A}$ and $T_{\text{top},B}$, respectively, associated with $s\tau\sigma \to s'\tau'\sigma'$ transitions, are thus related by

$$\tilde{t}_{s\tau,s'\tau'}^{\sigma,\sigma'} = ss' t_{-s\tau,-s'\tau'}^{\bar{\sigma},\bar{\sigma}'}, \tag{69}$$

with $\bar{A} = B$ and $\bar{B} = A$. We next describe the possible scattering mechanisms induced by an adatom on top of a $\circ$-sublattice site, $\circ = A, B$, by calculating corresponding cross sections $\sigma_{s\tau,s'\tau'}^{\circ}$. Since $T_{\text{top},A}$ transforms into $T_{\text{top},B}$ under $\mathcal{R}_y$, the following relation holds:

$$\sigma_{s\tau,s'\tau'}^{B}(\theta) = \sigma_{-s\tau,-s'\tau'}^{A}(-\theta), \tag{70}$$

so that we can focus on computing $\sigma_{s\tau,s'\tau'}^{A}(\theta)$ only.

From this perspective, we first describe the scattering mechanisms that do not conserve spin and valley. Equation (62) directly implies that intravalley spin-flip and spin-preserving intervalley scattering induced by top-position adatoms are isotropic mechanisms, as

$$\sigma_{s\tau,-s\tau}^{A} = \frac{k|t|^2}{8\pi} \tag{71}$$

and

$$\sigma_{s\tau,s-\tau}^{A} = \frac{k|a|^2}{8\pi}. \tag{72}$$

Unlike adatoms in the hollow position, top-position adatoms induce intervalley spin-flip scattering processes [see Eq. (37) and text therein]. In particular, for adatoms on the A sublattice, corresponding differential cross sections, for $s \neq s'$ and $\tau \neq \tau'$, are finite:

$$\sigma^{A}_{s\tau,s'\tau'}(\theta) = \frac{k|t|^2}{2\pi}\cos^2\left(\frac{\theta}{2}\right)\delta_{s+\tau}. \tag{73}$$

However, since (73) is an even function of θ, scattering mechanisms originating from top-position adatoms yield zero transverse currents, i.e., $J^{A\perp}_{s\tau,s'\tau'} = 0$, whenever $s \neq s'$ or $\tau \neq \tau'$. These general considerations are consistent with first-principles calculations showing that spin-relaxation rates in graphene are very sensitive to the adsorption site [46].

Next, we study spin-preserving intravalley scattering. Irrespective of the valley τ and spin s, T-matrix elements associated with the A sublattice $t^{A,A}_{s\tau,s\tau}$ are equal. This contrasts with $t^{B,B}_{s\tau,s\tau}$ elements, which generally verify

$$t^{B,B}_{\uparrow K,\uparrow K} = t^{B,B}_{\downarrow K',\downarrow K'} \neq t^{B,B}_{\uparrow K',\uparrow K'} = t^{B,B}_{\downarrow K,\downarrow K}. \tag{74}$$

As a result, spin-preserving intravalley-scattering cross sections for $\uparrow K$ and $\downarrow K'$ charge carriers differ from those for $\downarrow K$ and $\uparrow K'$ quasiparticles, and $\sigma_{s\tau,s\tau}(\theta)$ is determined by the conserved quantity $s+\tau$. We start by considering the $s+\tau = \pm 2$ case. We define $\mathcal{M}_2 = \mathcal{M}^{A}_{\uparrow K,\uparrow K} = \mathcal{M}^{A}_{\downarrow K',\downarrow K'}$ and $\varphi_2 = \varphi^{A}_{\uparrow K,\uparrow K} = \varphi^{A}_{\downarrow K',\downarrow K'}$, which verify

$$\mathcal{M}_2 = \frac{2|v_0+\lambda_{\rm so}|.|V_0 - wg|}{|1-Ug+2wg^2|.|1-g(v_0+\lambda_{\rm so})|} \tag{75}$$

and

$$\begin{aligned}\varphi_2 = {}& \arctan\left(\frac{U\,{\rm Im}\,g - 2w\,{\rm Im}(g^2)}{1-U\,{\rm Re}\,g + 2w\,{\rm Re}(g^2)}\right)\\ &+ \arctan\left(\frac{(v_0+\lambda_{\rm so})\,{\rm Im}\,g}{(v_0+\lambda_{\rm so})\,{\rm Re}\,g - 1}\right)\\ &+ \arctan\left(\frac{w\,{\rm Im}\,g}{w\,{\rm Re}\,g - V_0}\right)\\ &+\pi H(w\,{\rm Re}\,g - V_0) + \pi H[(v_0+\lambda_{\rm so})\,{\rm Re}\,g - 1]\\ &-\pi H[U\,{\rm Re}\,g - 2w\,{\rm Re}(g^2) - 1].\end{aligned} \tag{76}$$

The case of Dirac fermions for which $s+\tau = 0$ is markedly different. Denoting $\mathcal{M}_0 = \mathcal{M}^{A}_{\downarrow K,\downarrow K} = \mathcal{M}^{A}_{\uparrow K',\uparrow K'}$ and $\varphi_0 = \varphi^{A}_{\downarrow K,\downarrow K} = \varphi^{A}_{\uparrow K',\uparrow K'}$, we obtain

$$\mathcal{M}_0 = \frac{2|V_0 - wg||v_0 - \lambda_{\rm so} - 2wg|}{|1-Ug+2wg^2|^2} \tag{77}$$

and

$$\begin{aligned}\varphi_0 = {}& \arctan\left(\frac{w\,{\rm Im}\,g}{V_0 - w\,{\rm Re}\,g}\right) - \arctan\left(\frac{2w\,{\rm Im}\,g}{v_0 - \lambda_{\rm so} - 2w\,{\rm Re}\,g}\right)\\ &+\pi H(2w\,{\rm Re}\,g + \lambda_{\rm so} - v_0) - \pi H(w\,{\rm Re}\,g - V_0).\end{aligned} \tag{78}$$

Crucially, currents $J^{A\perp}_{\uparrow K,\uparrow K} + J^{A\perp}_{\uparrow K',\uparrow K'}$ and $J^{A\perp}_{\downarrow K,\downarrow K} + J^{A\perp}_{\downarrow K',\downarrow K'}$ are equal, so that spin-preserving intravalley scattering does not give rise to any transverse spin current. The same holds true for spin-preserving intravalley scattering induced by an adatom on the B sublattice, but due to relation (70),

$$J^{B\perp}_{s\tau,s\tau} = -J^{A\perp}_{-s\tau,-s\tau}. \tag{79}$$

However, the transverse charge current arising from scattering with a single top-position adatom on sublattice $\sigma = A,B$,

$$J^{\sigma\perp}_{C} = \sum_{s,\tau} J^{\sigma\perp}_{s\tau,s\tau}, \tag{80}$$

is generally nonzero, and Eq. (79) directly implies $J^{A\perp}_{Q} = -J^{B\perp}_{Q}$. Macroscopically, top-position adatoms thus give rise to the CHE, provided that the populations of adatoms on the A and B sublattices differ by type or number. Let us now study transverse charge currents $J^{\sigma\perp}_{C}$ in more detail. Using Eqs. (80), (30), and (23), we obtain

$$J^{\sigma\perp}_{C} = \mp\frac{k s_E v_F}{4}(\mathcal{M}_0\sin\varphi_0 + \mathcal{M}_2\sin\varphi_2), \tag{81}$$

with $-$ $(+)$ for adatoms on the A (B) sublattice. It is interesting to note that the magnitude of $J^{\sigma\perp}_{C}$ is modulated by $\mathcal{M}_0$ and $\mathcal{M}_2$, which are proportional to $|v_0 - \lambda_{\rm so} - 2wg|$ and $|v_0 + \lambda_{\rm so}|$, respectively. While the dependence on $\lambda_{\rm so}$ is expected—as spin-orbit interaction is a well-known cause of the anomalous Hall effect [47]—the dependence on v_0, a scalar potential acting on graphene triangular states $\Gamma^{\dagger}_{m,s}|0\rangle$, is more surprising. However, this v_0 dependence has a trivial geometrical explanation: the $v_0\pi_{B,A}$ term of Hamiltonian $\mathcal{H}^{A,B}_{\rm top}$ is the continuum-theory counterpart of the trigonal potential, which affects the three graphene p_z orbitals neighboring the adsorption site, and trigonal potentials clearly scatter charges anisotropically.

We next describe the energy dependence of $J^{\sigma\perp}_{C}$. In neutral graphene, phases φ_0 and φ_2 are null. However, they exhibit large resonances at finite Fermi energies, such that

$${\rm Re}\,g = 1/\omega_{i=1,2,3}, \tag{82}$$

where

$$\omega_1 = v_0 + \lambda_{\rm so}, \tag{83}$$

$$\omega_2 = v_0 - \lambda_{\rm so} - \frac{4\Lambda_{\rm so}^2}{V_0}, \tag{84}$$

$$\omega_3 = 2V_0 - \frac{8\Lambda_{\rm so}^2}{v_0 - \lambda_{\rm so}}. \tag{85}$$

Equation (82) has a low-energy root $|\mathcal{E}_i| \ll E_{\rm c}$ provided that $|\omega_i| \gg 2\pi E^2_{\hexagon}/E_{\rm c}$, in which case

$$\frac{\mathcal{E}_i}{E_{\rm c}} = \mathcal{L}\left(\frac{2\pi E^2_{\hexagon}}{E_{\rm c}\omega_i}\right). \tag{86}$$

Another resonance is reached whenever

$${\rm Re}(g^2) - \frac{U}{2w}{\rm Re}\,g + \frac{1}{2w} = 0. \tag{87}$$

Equation (87) admits a low-energy solution $\mathcal{E}_4$ verifying

$$\frac{\mathcal{E}_4}{E_{\rm c}} \approx \mathcal{L}\left(\frac{2\pi E^2_{\hexagon}}{E_{\rm c}U}\right), \tag{88}$$

provided $8|w| \ll U^2$ and $|U| \gg 2\pi E_{\rm c}$.

We now write conditions for the existence of resonant energies close to the Dirac point, in terms of tight-binding parameters connecting central and triangular states to the top-position adatoms. We first consider the marginal case of s-orbital adatoms, which only host states of total angular momentum $J = \pm 1/2$. Couplings between triangular states of angular momentum $m = \pm 1$ are thus necessarily mediated by double spin-flip through an available adatom orbital. Using the Appendix notations as well as Eqs. (A29) and (A31) within, this results in $v_0 = -\lambda_{\rm so} \approx -\frac{9}{2}\frac{l_{{\rm so},1}^2}{E_{1/2}^+}$ and $\Lambda_{\rm so} \approx -\frac{9}{2}\frac{l_{{\rm so},1}\gamma}{E_{1/2}^+}$. Therefore, $\omega_1 = 0$ and resonant energy $\mathcal{E}_1$ is infinite. In addition, the hopping integral $l_{{\rm so},1}$ connecting triangular states $\Gamma^\dagger_{\pm 1,\downarrow/\uparrow}|0\rangle$ to s orbitals of opposite spin is expected to be small compared to $E_{1/2}^+$ and graphene half-bandwidth $E_{\rm c}$, leading to $|\omega_{2,3}| \ll 2\pi E_{\hexagon}^2/E_{\rm c}$ and $|\mathcal{E}_{2,3}| \gg E_{\rm c}$. Resonant energies $\mathcal{E}_{1,2,3}$ are thus experimentally irrelevant. However, $U \approx -2\gamma^2/E_{1/2}^+$ and $\mathcal{E}_4$ is the only resonance that can possibly be observed, provided $\gamma^2/|E_{1/2}^+| \gg \pi E_{\rm c}$.

For all other types of valence orbitals, i.e., p, d, and f, the existence of spin-preserving channels coupling triangular states of angular momentum $m = \pm 1$ gives rise to enhanced v_0, $\lambda_{\rm so}$, and $\Lambda_{\rm so}$ energy scales, making resonant energies $\mathcal{E}_{i=1,2,3}$ accessible under certain conditions. Equations (A29) and (A31) lead directly to

$$V_0 \sim -\frac{\gamma^2}{E_{1/2}^+}, \tag{89}$$

$$v_0 \sim -\frac{9}{2}\theta_1^2\left(\frac{1}{E_{1/2}^-} + \frac{1}{E_{3/2}^+}\right), \tag{90}$$

$$\lambda_{\rm so} \sim \frac{9}{2}\theta_1^2\left(\frac{1}{E_{1/2}^-} - \frac{1}{E_{3/2}^+}\right), \tag{91}$$

$$\Lambda_{\rm so} \sim -\frac{9}{2}\frac{\gamma\theta_1\Lambda_{\rm so}^1}{E_{1/2}^-E_{1/2}^+}. \tag{92}$$

Therefore, Eq. (82) holds for $i = 1, 2$, or 3 if $\theta_1^2/|E_{3/2}^+| \gg E_{\hexagon}^2/E_{\rm c}$, $\theta_1^2/|E_{1/2}^-| \gg E_{\hexagon}^2/E_{\rm c}$, or $\gamma^2/|E_{1/2}^+| \gg 2\pi E_{\hexagon}^2/E_{\rm c}$, respectively. Moreover,

$$U \sim -\frac{2\gamma^2}{E_{1/2}^+} - \frac{9\theta_1^2}{E_{1/2}^-}, \tag{93}$$

and assuming $\Lambda_{\rm so}$ is much smaller than V_0, v_0, and $\lambda_{\rm so}$, we have

$$w \sim \frac{9\theta_1^2\gamma^2}{E_{1/2}^-E_{1/2}^+}, \tag{94}$$

so that Eq. (88) is valid provided $|\gamma| \gg |\theta_1|$ or $|\gamma| \ll |\theta_1|$, and $2\gamma^2/|E_{1/2}^+| + 9\theta_1^2/|E_{1/2}^-| \gg 2\pi E_{\hexagon}^2/E_{\rm c}$.

Figure 8(a) shows the transverse charge current $J_C^{A\perp}$ as a fraction of total outgoing current,

$$J_C^{A\parallel} = s_E v_F \sum_{s,\tau,s',\tau'} \Sigma^{A\parallel}_{s\tau,s'\tau'}, \tag{95}$$

against Fermi energy E_F, for fixed values of atomic energy levels $E_{1/2}^\pm$, and $E_{3/2}^\pm$, and various (γ,θ_1) points, labeled as A, B, C, D, and E. While for small γ and θ_1 (situation A) the transverse charge current is negligible compared to $J_C^{A\parallel}$, significant $J_C^{A\perp}$ currents are obtained for values of γ and θ_1 of the order of a few eV [points B, C, D, E in Fig. 8(b)], up to 20%. In addition, the transverse charge current can change direction for some values of Fermi energy, as illustrated by curves C and E in Fig. 8(a). Such "inversion" energies can exist close to the Dirac point for finite values of γ and θ_1 only. Denoting as $\mathcal{E}_{\rm inv}$ the inversion energy closest to the Dirac point for a given (γ,θ_1) couple, Fig. 8(b) shows $|\mathcal{E}_{\rm inv}(\gamma,\theta_1)| = E_{\rm c}/10$ lines, which partition (γ,θ_1) space into regions whose farthest point from the origin corresponds to $|\mathcal{E}_{\rm inv}|/E_{\rm c} < 0.1$. Clearly, $|\mathcal{E}_{\rm inv}|/E_{\rm c} < 0.1$, domains overlap with regions of large $J_C^{A\perp}/J_C^{A\parallel}$ magnitude, making the existence of $\mathcal{E}_{\rm inv}$ relevant for applications. Similar to transverse spin currents arising from scattering with hollow-position adatoms, we believe

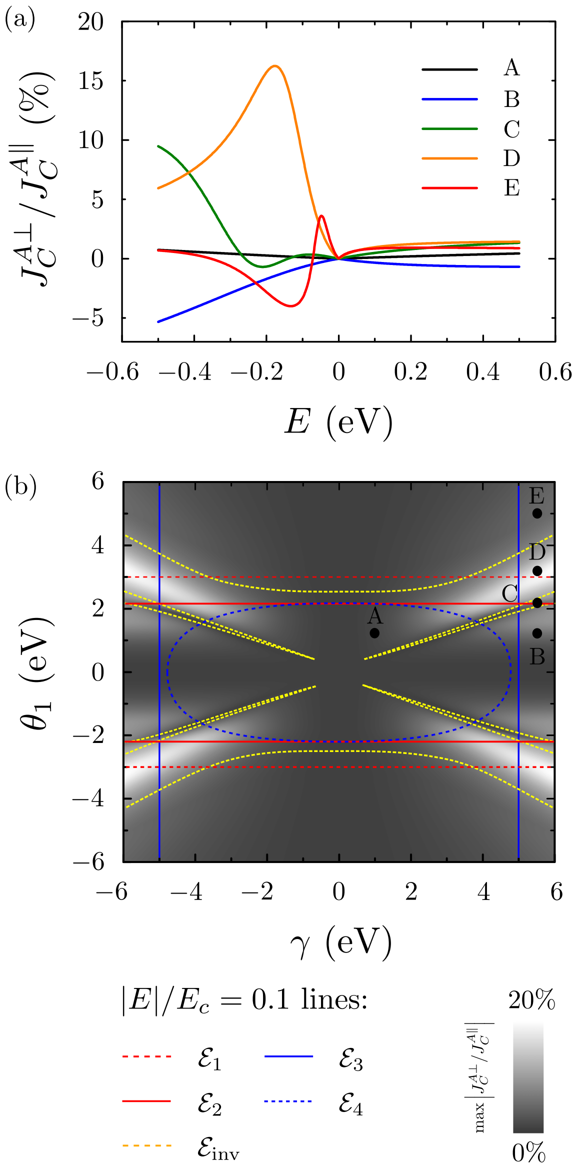

FIG. 8. (Color online) Resonant features of charge transverse currents generated by top-position physisorbed adatoms on graphene. (a) $J_C^{A\perp}/J_C^{A\parallel}$ (in %) against Fermi energy (in eV), for top-position adatoms with fixed $E_{1/2}^\pm = -1$ eV and $E_{3/2}^\pm = -1.5$ eV and different (γ,θ_1), corresponding to points A, B, C, D, and E shown in the lower panel. (b) Maximum of $|J_C^{A\perp}/J_C^{A\parallel}|$ for $|E_F| \leqslant 0.5$ eV, against γ and θ_1. $|E|/E_{\rm c} = 0.1$ lines are shown for $E = \mathcal{E}_{1,2,3,4},\mathcal{E}_{\rm inv}$. Similarly to Fig. 7, each line partitions (γ,θ_1) space into regions whose farthest point from the origin corresponds to $|E|/E_{\rm c} < 0.1$.

that the possibility of changing the sign of $J_Q^{\sigma\perp}$ by a field effect could be explored for new functionalities in logic devices. At the scale of an entire graphene device, however, the observation of significant macroscopic transverse charge currents due to scattering with a large ensemble of top-position adatoms appears more challenging than the observation of a large SHE due to hollow-position adatoms because of the necessity of having an imbalance between the A and B sublattices. Nevertheless, it should be noted that sublattice ordering driven by Ruderman-Kittel-Kasuya-Yosida (RKKY) -type interactions below a critical temperature was predicted by several authors [48–51], so that the above-discussed CHE may in principle be observed in an experiment.

IV. CONCLUDING REMARKS

In this work, we have provided a rigorous derivation of effective graphene-adatom Hamiltonians, taking into account intervalley terms neglected in previous works. Our results describe the experimentally relevant scenario of dilute physically adsorbed adatoms randomly distributed over the graphene lattice. We have shown that both the position in the lattice and the valence orbital type are critical to determine the action of a physisorbed adatom on graphene's Dirac fermions. Our study of nonmagnetic elements—valid when the Fermi energy is detuned from the adatoms' valence orbital spectrum—established that while bridge-position adsorption does not induce spin-orbit coupling, hollow- and top-position adatoms can generate significant local spin-orbit interactions in such a way that spin and valley quantum numbers are strongly intertwined. The low-energy continuum theories constructed for hollow- and top-position species allowed us to obtain analytic expressions for T matrices and integrated cross sections and to derive the corresponding charge carriers' spin-dependent scattering mechanisms. Interestingly, hollow- and top-position spin-orbit active adatoms give rise to Hall effects of drastically different nature: pure spin currents for the former (SHE), and nonpolarized charge currents for the latter (CHE). They nonetheless have two key characteristics in common: they can be switched on and off and their flow can be reversed by tuning the Fermi energy. We anticipate that such properties will find technological applications in the fields of spin- and charge-based logic components.

ACKNOWLEDGMENTS

The authors wish to thank N. M. R. Peres, J. M. B. L. dos Santos, V. M. Pereira, M. A. Cazalilla, and T. G. Rappoport for helpful discussions. We also wish to thank V. M. Pereira for pointing out Ref. [38] to us. A.P., A.F., and A.H.C.N. acknowledge support from National Research Foundation–Competitive Research Programme through the grant "Novel 2D materials with tailored properties: beyond graphene" (Grant No. R-144-000-295-281). A.P. and B.O. acknowledge support from Singapore Millennium Foundation–NUS Research Horizons award (R-144-001-271-592, R-144-001-271-646).

APPENDIX

In this appendix, we rederive the impurity Hamiltonians of Sec. I for adatoms in the hollow and top positions, accounting for internal degrees of freedom. We describe the graphene-adatom system with a tight-binding Hamiltonian $H = H_{\rm gr} + H_{\rm ad} + V$, where $H_{\rm gr}$ is pristine graphene's Hamiltonian, $H_{\rm ad}$ is the adatoms' Hamiltonian, and V is the graphene-adatom hybridization term. We write $H_{\rm gr}$ as the following first-nearest-neighbor tight-binding Hamiltonian:

$$H_{\rm gr} = -t \sum_{i\in\mathcal{A}} \sum_{\langle i,j\rangle} a_i^\dagger b_j + \text{H.c.}, \tag{A1}$$

where $\mathcal{A}$ denotes graphene's A-sublattice carbon atoms, and $a_i^\dagger$ (b_j) creates an A-sublattice electron at atom $i \in \mathcal{A}$ (annihilates an electron from the B-sublattice site j). Here, $\langle i,j\rangle$ refers to nearest neighbors j of site i, and t is the hopping energy between nearest neighbors. Next, we derive single-electron tight-binding Hamiltonians for $H_{\rm ad}$ and V by invoking symmetry arguments [15], and then we trace out the adatom degrees of freedom via the Löwdin transformation [52]. Taking the continuum limit then yields the results of Table I. In addition to confirming the results obtained in Sec. I, this approach has the advantage of relating couplings (V_0, $V_{\rm so}$, Δ, $\Delta_{\rm so}$, $\Lambda_R, \ldots$) appearing in Table I to microscopic parameters (hopping integrals, atomic spin-orbit couplings, and energy levels) and the Fermi energy of graphene.

We start by writing the solution of the Schrödinger equation $H|\psi\rangle = E|\psi\rangle$ as a sum of waves $|\psi\rangle = |\psi_{\rm ad}\rangle + |\psi_{\mathcal{N}}\rangle + |\psi_\infty\rangle$, where $|\psi_{\rm ad}\rangle$, $|\psi_{\mathcal{N}}\rangle$, and $|\psi_\infty\rangle$ are projections of $|\psi\rangle$ on the adatom valence l orbital, its immediate vicinity—where graphene's p_z orbitals couple strongly to the adatom's valence orbital—and graphene's distant p_z orbitals, respectively (see Fig. 9). We denote by $d_{m,s}^\dagger$ the operator creating an adatom's l orbital of angular momentum m and spin s, and we write $d_{m,s}^\dagger|0\rangle = |m,s\rangle_{\rm ad}$. In the case of an adatom in the hollow

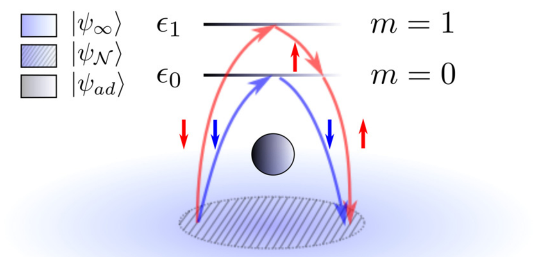

FIG. 9. (Color online) Illustration of typical spin-flip (red) and spin-conserving (blue) processes induced by a p-orbital adatom (gray) on graphene (light blue). Energy levels ϵ_0 and ϵ_1 of the adatom's p orbitals $m = 0$ and $m = \pm 1$ are represented as gray solid lines. Core orbitals are depicted as a black ball. The shaded region corresponds to the adatom's immediate vicinity, where carbon atom p_z orbitals couple strongly to the adatom valence p orbital. Red (blue) straight vertical arrows represent the spin of an electron transiting between graphene and the adatom while flipping (conserving) its spin. Partial waves $|\psi_\infty\rangle$, $|\psi_{\mathcal{N}}\rangle$, and $|\psi_{\rm ad}\rangle$ introduced in the Appendix are associated with the blue area, the dashed area, and the adatom's valence orbital, respectively.

position, $|\psi_{\mathcal{N}}\rangle$ is a linear combination of hexagonal states, $\Omega^\dagger_{m,s}|0\rangle = |m,s\rangle_{\mathcal{N}}$. For top-position adatoms, $|\psi_{\mathcal{N}}\rangle$ is a linear combination of triangular states, $\Gamma^\dagger_{m,s}|0\rangle$ and $c_0^\dagger|0\rangle$. Here, we explain the method used in the case of an adatom in the hollow position, the top-position treatment case being analogous. We write $|\psi_{\text{ad}}\rangle$ and $|\psi_{\mathcal{N}}\rangle$ as

$$|\psi_{\mathcal{N}}\rangle = \sum_{s,m} \alpha_{m,s}|m,s\rangle_{\mathcal{N}}, \tag{A2}$$

$$|\psi_{\text{ad}}\rangle = \sum_{s,m} \beta_{m,s}|m,s\rangle_{\text{ad}}. \tag{A3}$$

The projection of the Schrödinger equation $H|\psi\rangle = E|\psi\rangle$ on $|m,s\rangle_{\text{ad}}$ gives

$$\sum_{s',m'} \beta_{m',s'\,\text{ad}}\langle m,s|H_{\text{ad}}|m',s'\rangle_{\text{ad}} + \sum_{s',m'} \alpha_{m',s'\,\text{ad}}\langle m,s|V|m',s'\rangle_{\mathcal{N}}$$
$$= \beta_{m,s}\delta_{m,m'}\delta_{s,s'}E. \tag{A4}$$

To proceed, we denote by $\hat{\mathcal{Z}}$ the matrix with elements $({}_{\text{ad}}\langle m,s|H_{\text{ad}}|m',s'\rangle_{\text{ad}})_{(m,s),(m',s')}$ and by $\hat{\mathcal{T}}$ the matrix with elements $({}_{\text{ad}}\langle m,s|V|m',s'\rangle_{\mathcal{N}})_{(m,s),(m',s')}$. Within this notation, Eq. (A4) is recast into the elegant form

$$B = (E\mathbb{I} - \hat{\mathcal{Z}})^{-1}\hat{\mathcal{T}}A, \tag{A5}$$

where A and B are vectors with components $(\alpha_{m,s})_{(m,s)}$ and $(\beta_{m,s})_{(m,s)}$, respectively. Setting $H_{\text{imp}} = H_{\text{ad}} + V$, we next project the vector $H_{\text{imp}}|\psi\rangle$ on $|m,s\rangle_{\mathcal{N}}$ states. This gives

$${}_{\mathcal{N}}\langle m,s|H_{\text{imp}}|\psi\rangle = \sum_{m',s'} \alpha_{m',s'\,\mathcal{N}}\langle m,s|\hat{\mathcal{S}}|m',s'\rangle_{\text{ad}}, \tag{A6}$$

where

$$\hat{\mathcal{S}} = \hat{\mathcal{T}}^\dagger(E\mathbb{I} - \hat{\mathcal{Z}})^{-1}\hat{\mathcal{T}}. \tag{A7}$$

Equation (A6) can be interpreted as the projection of the vector $\tilde{H}_{\text{imp}}(|\psi\rangle_{\mathcal{N}} + |\psi\rangle_\infty)$ on the state $|m,s\rangle_{\mathcal{N}}$, where $\tilde{H}_{\text{imp}}$ is the *graphene-only* Hamiltonian:

$$\tilde{H}_{\text{imp}} = \sum_{m,s}\sum_{m',s'} \hat{\mathcal{S}}_{(m,s),(m',s')}\Omega^\dagger_{m,s}\Omega_{m',s'}. \tag{A8}$$

Tracing H_{ad} out hence consists in replacing H_{imp} by $\tilde{H}_{\text{imp}}$ in the full Hamiltonian H.

We now derive a single-electron tight-binding Hamiltonian H_{ad} describing an l-orbital adatom either in the hollow or top position, thereby generalizing a result of Ref. [15] for p orbitals. We start with an ansatz Hamiltonian H_{ad} that manifestly conserves the total angular momentum,

$$H_{\text{ad}} = \sum_{m=-l}^{l} \epsilon_m d^\dagger_m d_m + \sum_{m=-l}^{l} \lambda^m_{\text{so}} d^\dagger_m s_z d_m$$
$$+ \sum_{m=-l}^{l-1} \Lambda^m_{\text{so}}(d^\dagger_m s_+ d_{m+1} + d^\dagger_{m+1} s_- d_m). \tag{A9}$$

This Hamiltonian is invariant under rotation by $\pi/3$, so that choosing energies ϵ_m, λ^m_{so}, and Λ^m_{so}, such that H_{ad} is time-reversal invariant and symmetric under $\mathcal{R}_x : x \mapsto -x$ reflection, makes it suitable for describing *both* hollow- and top-position l-orbital adatoms, $l = p,d,f$. Since in spherical coordinates $\langle\theta,\phi|d^\dagger_m|0\rangle = Y^m_l(\theta,\phi)$, where $Y^m_l(\theta,\phi)$ are conventional spherical harmonics, d_m transforms into $s_x d_{-m}$ under $\mathcal{R}_x$, which sends ϕ to $\pi - \phi$. Enforcing $\mathcal{R}_x$ symmetry thus requires $\epsilon_m = \epsilon_{-m}$, $\lambda^{-m}_{\text{so}} = -\lambda^m_{\text{so}}$, and $\Lambda^{-m-1}_{\text{so}} = \Lambda^m_{\text{so}}$. Moreover, time-reversal symmetry requires ϵ_m, λ^m_{so}, and Λ^m_{so} to be real. We end up with

$$H_{\text{ad}} = \sum_{m=-l}^{l} \epsilon_{|m|} d^\dagger_m d_m + \sum_{m=1}^{l} \lambda^m_{\text{so}}(d^\dagger_m s_z d_m - d^\dagger_{-m} s_z d_{-m})$$
$$+ \sum_{m=0}^{l-1} \Lambda^m_{\text{so}}(d^\dagger_m s_+ d_{m+1} + d^\dagger_{-m-1} s_+ d_{-m} + \text{H.c.}), \tag{A10}$$

which describes the adatom Hamiltonian for both the hollow and top positions. However, hybridization terms V differ in the hollow- and top-position cases. We first treat the hollow-position situation, in which total angular momentum conservation constrains V to take the form

$$V_{\text{hollow}} = \sum_{m=-2}^{2} t_m d^\dagger_m \Omega_m + \sum_{m=-2}^{2} \tau_m d^\dagger_m s_z \Omega_m$$
$$+ \sum_{m=-2}^{2} \left(W^m_{\text{so}} d^\dagger_{m-1} s_+ \Omega_m + V^m_{\text{so}} d^\dagger_{m+1} s_- \Omega_m\right) + \text{ H.c.} \tag{A11}$$

Since $\Omega_m \mapsto s_x\Omega_{-m}$ under $\mathcal{R}_x$, we must have $t_m = t_{-m}$, $\tau_m = -\tau_{-m}$, and $W^m_{\text{so}} = V^{-m}_{\text{so}}$. Enforcing time-reversal symmetry requires t_m, τ_m, and W^m_{so} to read $t_m = i^{|m|}u_{|m|}$, $\tau_m = i^m v_{|m|}$, and $W^m_{\text{so}} = i^m w_m$, where $u_{|m|}$, $v_{|m|}$, and w_m are real. Finally,

$$V_{\text{hollow}} = \sum_{m=-2}^{2} i^{|m|}u_{|m|} d^\dagger_m \Omega_m$$
$$+ \sum_{m=1}^{2} i^m v_{|m|}(d^\dagger_m s_z \Omega_m - d^\dagger_{-m} s_z \Omega_{-m})$$
$$+ \sum_{m=-2}^{2} i^m w_m(d^\dagger_{m-1} s_+ \Omega_m + d^\dagger_{-m+1} s_- \Omega_{-m}) + \text{H.c.} \tag{A12}$$

A similar treatment allows us to derive V for top-position adatoms. Enforcing symmetry under $\mathcal{R}_x$, time-reversal symmetry, and total angular momentum conservation, we obtain

$$V_{\text{top}} = \sum_{m=-1}^{1} i^{|m|}\theta_{|m|} d^\dagger_m \Gamma_m + i\tau(d^\dagger_1 s_z \Gamma_1 - d^\dagger_{-1} s_z \Gamma_{-1})$$
$$+ \sum_{m=0,1} i^m l_{\text{so,m}}(d^\dagger_{m-1} s_+ \Gamma_m + d^\dagger_{-m+1} s_- \Gamma_{-m})$$
$$+ L_{\text{so}}(d^\dagger_{-1} s_+ c_0 + d^\dagger_1 s_- c_0) + \gamma d^\dagger_0 c_0 + \text{H.c.}, \tag{A13}$$

where θ_m, τ, $l_{\text{so,m}}$, L_{so}, and γ are real. We can now derive graphene-only Hamiltonians for adatoms in the hollow or top position using Eqs. (A7) and (A8). We write the $\hat{\mathcal{Z}}$ matrix, similar for both hollow- and top-position adatoms in a basis $\mathcal{B}_l$ of $2(2l+1)$ states $|m,s\rangle_{\text{ad}}$ arranged in ascending total angular momentum $J = m + s$ order:

$$\begin{aligned}\mathcal{B}_l = \{&|-l,\downarrow\rangle_{\text{ad}},|-l,\uparrow\rangle_{\text{ad}},|-l+1,\downarrow\rangle_{\text{ad}},\\ &|-l+1,\uparrow\rangle_{\text{ad}},\ldots,|l,\downarrow\rangle_{\text{ad}},|l,\uparrow\rangle_{\text{ad}}\}.\end{aligned} \tag{A14}$$

In basis $\mathcal{B}_l$, the $\hat{\mathcal{Z}}$ matrix is simply block-diagonal and reads

$$\hat{\mathcal{Z}} = \begin{pmatrix} \hat{\mathcal{Z}}_{-l-\frac{1}{2}} & 0 & \cdots & 0 & 0 \\ 0 & \hat{\mathcal{Z}}_{-l+\frac{1}{2}} & \cdots & 0 & 0 \\ \vdots & \vdots & \ddots & \vdots & \vdots \\ 0 & 0 & \cdots & \hat{\mathcal{Z}}_{l-\frac{1}{2}} & 0 \\ 0 & 0 & \cdots & 0 & \epsilon_l + \lambda_{\text{so}}^l \end{pmatrix}, \tag{A15}$$

where $\hat{\mathcal{Z}}_{-l-\frac{1}{2}} = \hat{\mathcal{Z}}_{l+\frac{1}{2}} = \epsilon_l + \lambda_{\text{so}}^l$. If $|J| \neq l + \frac{1}{2}$, then $\hat{\mathcal{Z}}_J$ are 2×2 matrices acting on total-angular momentum J subspace:

$$\hat{\mathcal{Z}}_J = \begin{pmatrix} E_J^+ & \Delta_J \\ \Delta_J & E_J^- \end{pmatrix}, \tag{A16}$$

where $E_J^{\pm} = \epsilon_{s_J(J\mp\frac{1}{2})} \pm s_J \lambda_{\text{so}}^{s_J(J\mp\frac{1}{2})}$, $\Delta_J = \Lambda_{\text{so}}^{|J|+\frac{1}{2}}$, $s_J = J/|J|$, and $\lambda_{\text{so}}^0 = 0$. Using basis $\mathcal{B}_\Omega$ of hexagonal states in ascending-J order,

$$\begin{aligned}\mathcal{B}_\Omega = \{&|-2,\downarrow\rangle_{\mathcal{N}},|-2,\uparrow\rangle_{\mathcal{N}},|-1,\downarrow\rangle_{\mathcal{N}},\\ &|-1,\uparrow\rangle_{\mathcal{N}},\ldots,|2,\downarrow\rangle_{\mathcal{N}},|2,\uparrow\rangle_{\mathcal{N}}\},\end{aligned} \tag{A17}$$

the "hybridization" matrix $\hat{\mathcal{T}}$ for a hollow-position adatom is also a sparse matrix. Its only nonzero elements are in 2×2 and 1×2 blocks $\hat{\mathcal{T}}_J$ connecting subspaces of hexagonal and adatom orbital states of same total angular momentum J. The 2×2 $\hat{\mathcal{T}}_J$ blocks read

$$\hat{\mathcal{T}}_J = i^{J-\frac{1}{2}} \begin{pmatrix} a_J u_{|J-\frac{1}{2}|} + v_{|J-\frac{1}{2}|} & i w_{J+\frac{1}{2}} \\ i^{-2J+1} w_{-J+\frac{1}{2}} & b_J u_{|J+\frac{1}{2}|} + i v_{|J+\frac{1}{2}|} \end{pmatrix}, \tag{A18}$$

where $a_J = i^{|J-\frac{1}{2}|-J+\frac{1}{2}}$ and $b_J = i^{|J+\frac{1}{2}|-J+\frac{1}{2}}$, while 1×2 blocks are appropriate submatrices of the 2×2 blocks shown in Eq. (A18). As a result, the $\hat{\mathcal{S}}$ matrix is block-diagonal and, for instance, the f-orbital adatom graphene-only Hamiltonian reads

$$\tilde{H}_{\text{hollow}} = \sum_{m=-l}^{l} (\Omega_{m\uparrow}^\dagger, \Omega_{m+1\downarrow}^\dagger) \hat{\mathcal{S}}_{m+\frac{1}{2}} \begin{pmatrix} \Omega_{m\uparrow} \\ \Omega_{m+1\downarrow} \end{pmatrix}, \tag{A19}$$

with

$$\hat{\mathcal{S}}_J = \hat{\mathcal{T}}_J^\dagger (E\mathbb{I} - \hat{\mathcal{Z}}_J)^{-1} \hat{\mathcal{T}}_J. \tag{A20}$$

Similar results are straightforwardly obtained for p- and d-orbital adatoms. The connection with the Hamiltonian of Eq. (2) is easily made, as

$$\hat{\mathcal{S}}_{m+\frac{1}{2}} = \begin{pmatrix} \nu_m^+ + \nu_m^- & i\Lambda_m \\ -i\Lambda_m & \nu_{m+1}^+ - \nu_{m+1}^- \end{pmatrix}. \tag{A21}$$

We now write the "hybridization" matrix $\hat{\mathcal{T}}_{\text{top}}$ for top-position adatoms, using a basis $\mathcal{B}_{\text{top}}$ of states arranged in ascending-J order:

$$\begin{aligned}\mathcal{B}_{\text{top}} = \{&\Gamma_{-1,\downarrow}^\dagger|0\rangle,\Gamma_{-1,\uparrow}^\dagger|0\rangle,\Gamma_{0,\downarrow}^\dagger|0\rangle,c_{0,\downarrow}^\dagger|0\rangle,\\ &c_{0,\uparrow}^\dagger|0\rangle,\Gamma_{0,\uparrow}^\dagger|0\rangle,\Gamma_{1,\downarrow}^\dagger|0\rangle,\Gamma_{1,\uparrow}^\dagger|0\rangle\}.\end{aligned} \tag{A22}$$

Unlike $\mathcal{B}_\Omega$, $\mathcal{B}_{\text{top}}$ comprises six states of total angular momentum $\pm 1/2$ due to the presence of central states $c_{0,\uparrow/\downarrow}^\dagger|0\rangle$ in addition to triangular states $\Gamma_{0,\uparrow/\downarrow}^\dagger|0\rangle$. Correspondingly, the only nonzero elements of $\hat{\mathcal{T}}_{\text{top}}$ are in blocks $\hat{\mathcal{T}}_{\text{top},J}$ connecting states of total angular momentum J. Irrespective of the adatom's valence orbital—p, d, or f—we have

$$\hat{\mathcal{T}}_{\text{top},-\frac{1}{2}} = \begin{pmatrix} i\theta_{-1} + i\tau & l_{\text{so},0} & L_{\text{so}} \\ i l_{\text{so},1} & \theta_0 & \gamma \end{pmatrix}, \tag{A23}$$

$$\hat{\mathcal{T}}_{\text{top},\frac{1}{2}} = \begin{pmatrix} \gamma & \theta_0 & i l_{\text{so},1} \\ L_{\text{so}} & l_{\text{so},0} & i\theta_1 - i\tau \end{pmatrix}. \tag{A24}$$

Other blocks $\hat{\mathcal{T}}_{\text{top},J}$ depend on the adatom's valence orbital, but are appropriate subarrays of

$$\hat{\mathcal{T}}_{\text{top},-\frac{3}{2}} = \begin{pmatrix} -i l_{\text{so},-1} \\ i\theta_1 + i\tau \end{pmatrix}, \tag{A25}$$

$$\hat{\mathcal{T}}_{\text{top},\frac{3}{2}} = \begin{pmatrix} i\theta_1 + i\tau \\ -i l_{\text{so},-1} \end{pmatrix}. \tag{A26}$$

The $\hat{\mathcal{S}}$ matrix for top-position adatoms is block-diagonal,

$$\hat{\mathcal{S}}_{\text{top}} = \begin{pmatrix} \hat{\mathcal{S}}_{\text{top},-\frac{3}{2}} & 0 & 0 & 0 \\ 0 & \hat{\mathcal{S}}_{\text{top},-\frac{1}{2}} & 0 & 0 \\ 0 & 0 & \hat{\mathcal{S}}_{\text{top},\frac{1}{2}} & 0 \\ 0 & 0 & 0 & \hat{\mathcal{S}}_{\text{top},\frac{3}{2}} \end{pmatrix}, \tag{A27}$$

with $\hat{\mathcal{S}}_{\text{top},J} = \hat{\mathcal{T}}_{\text{top},J}^\dagger (E\mathbb{I} - \hat{\mathcal{Z}}_J)^{-1} \hat{\mathcal{T}}_{\text{top},J}$ as in Eq. (A20). The graphene-only top-position Hamiltonian thus reads

$$\begin{aligned}\tilde{H}_{\text{top}} = {}& \hat{\mathcal{S}}_{\text{top},-\frac{3}{2}} \Gamma_{-1,\downarrow}^\dagger \Gamma_{-1,\downarrow} + \hat{\mathcal{S}}_{\text{top},\frac{3}{2}} \Gamma_{1,\uparrow}^\dagger \Gamma_{1,\uparrow} \\ & + (\Gamma_{-1,\uparrow}^\dagger, \Gamma_{0,\downarrow}^\dagger, c_{0,\downarrow}^\dagger) \hat{\mathcal{S}}_{\text{top},-\frac{1}{2}} \begin{pmatrix} \Gamma_{-1,\uparrow} \\ \Gamma_{0,\downarrow} \\ c_{0,\downarrow} \end{pmatrix} \\ & + (c_{0,\uparrow}^\dagger, \Gamma_{0,\uparrow}^\dagger, \Gamma_{1,\downarrow}^\dagger) \hat{\mathcal{S}}_{\text{top},\frac{1}{2}} \begin{pmatrix} c_{0,\uparrow} \\ \Gamma_{0,\uparrow} \\ \Gamma_{1,\downarrow} \end{pmatrix}.\end{aligned} \tag{A28}$$

This is exactly the Hamiltonian of Eq. (9) with the following correspondence:

$$\hat{\mathcal{S}}_{\text{top},-\frac{3}{2}} = \hat{\mathcal{S}}_{\text{top},\frac{3}{2}} = \Lambda_+ + \Lambda_-, \tag{A29}$$

$$\hat{\mathcal{S}}_{\text{top},-\frac{1}{2}} = \begin{pmatrix} \Lambda_+ - \Lambda_- & -i\tau & -i\mu \\ i\tau & V_1 & V_2 \\ i\mu & V_2 & V_0 \end{pmatrix}, \tag{A30}$$

and

$$\hat{\mathcal{S}}_{\text{top},\frac{1}{2}} = \begin{pmatrix} V_0 & V_2 & i\mu \\ V_2 & V_1 & i\tau \\ -i\mu & -i\tau & \Lambda_+ - \Lambda_- \end{pmatrix}. \tag{A31}$$

[1] K. S. Novoselov, A. K. Geim, S. V. Morozov, D. Jiang, Y. Zhang, S. V. Dubonos, I. V. Grigorieva, and A. A. Firsov, Science **306**, 666 (2004).

[2] A. H. Castro Neto, F. Guinea, N. M. R. Peres, K. S. Novoselov, and A. K. Geim, Rev. Mod. Phys. **81**, 109 (2009).

[3] J. P. Hobson and W. A. Nierenberg, Phys. Rev. **89**, 662 (1953).

[4] N. M. R. Peres, F. Guinea, and A. H. Castro Neto, Phys. Rev. B **73**, 125411 (2006).

[5] T. Ando, J. Phys. Soc. Jpn. **75**, 074716 (2006).

[6] K. S. Novoselov, A. K. Geim, S. V. Morozov, D. Jiang, M. I. Katsnelson, I. V. Grigorieva, S. V. Dubonos, and A. A. Firsov, Nature (London) **438**, 197 (2005).

[7] A. Pachoud, M. Jaiswal, P. K. Ang, K. P. Loh, and B. Özyilmaz, Europhys. Lett. **92**, 27001 (2010).

[8] D. K. Efetov and P. Kim, Phys. Rev. Lett. **105**, 256805 (2010).

[9] R. R. Nair, M. Sepioni, I. L. Tsai, O. Lehtinen, J. Keinonen, A. V. Krasheninnikov, T. Thomson, A. K. Geim, and I. V. Grigorieva, Nat. Phys. **8**, 199 (2012).

[10] R. R. Nair, I.-L. Tsai, M. Sepioni, O. Lehtinen, J. Keinonen, A. V. Krasheninnikov, A. H. Castro Neto, M. I. Katsnelson, A. K. Geim, and I. V. Grigorieva, Nat. Commun. **4**, 2010 (2013).

[11] B. Uchoa, V. N. Kotov, N. M. R. Peres, and A. H. Castro Neto, Phys. Rev. Lett. **101**, 026805 (2008).

[12] R. R. Nair, W. Ren, R. Jalil, I. Riaz, V. G. Kravets, L. Britnell, P. Blake, F. Schedin, A. S. Mayorov, S. Yuan, M. I. Katsnelson, H. M. Cheng, W. Strupinski, L. G. Bulusheva, A. V. Okotrub, I. V. Grigorieva, A. N. Grigorenko, K. S. Novoselov, and A. K. Geim, Small **6**, 2877 (2010).

[13] A. Pachoud, M. Jaiswal, Y. Wang, B. H. Hong, J. H. Ahn, K. P. Loh, and B. Özyilmaz, Sci. Rep. **3**, 3404 (2013).

[14] A. H. Castro Neto and F. Guinea, Phys. Rev. Lett. **103**, 026804 (2009).

[15] C. Weeks, J. Hu, J. Alicea, M. Franz, and R. Wu, Phys. Rev. X **1**, 021001 (2011).

[16] M. Gmitra, D. Kochan, and J. Fabian, Phys. Rev. Lett. **110**, 246602 (2013).

[17] D. Marchenko, A. Varykhalov, M. R. Scholz, G. Bihlmayer, E. I. Rashba, A. Rybkin, A. M. Shikin, and O. Rader, Nat. Commun. **3**, 1232 (2012).

[18] J. Balakrishnan, G. Kok Wai Koon, M. Jaiswal, A. H. Castro Neto, and B. Özyilmaz, Nat. Phys. **9**, 284 (2013).

[19] D. A. Abanin, R. V. Gorbachev, K. S. Novoselov, A. K. Geim, and L. S. Levitov, Phys. Rev. Lett. **107**, 096601 (2011).

[20] O. V. Yazyev and M. I. Katsnelson, Phys. Rev. Lett. **100**, 047209 (2008).

[21] M. I. Dyakonov and V. I. Perel, JETP Lett. **13**, 467 (1971); J. E. Hirsch, Phys. Rev. Lett. **83**, 1834 (1999); S. Zhang, *ibid.* **85**, 393 (2000).

[22] T. Ando and T. Nakanishi, J. Phys. Soc. Jpn. **67**, 1704 (1998); V. M. Pereira, F. Guinea, J. M. B. Lopes dos Santos, N. M. R. Peres, and A. H. Castro Neto, Phys. Rev. Lett. **96**, 036801 (2006); D. S. Novikov, Phys. Rev. B **76**, 245435 (2007); T. Stauber, N. M. R. Peres, and F. Guinea, *ibid.* **76**, 205423 (2007); T. O. Wehling, A. V. Balatsky, M. I. Katsnelson, A. I. Lichtenstein, K. Scharnberg, and R. Wiesendanger, *ibid.* **75**, 125425 (2007); C. Bena, Phys. Rev. Lett. **100**, 076601 (2008); D. M. Basko, Phys. Rev. B **78**, 115432 (2008).

[23] A. Ferreira, J. Viana-Gomes, J. Nilsson, E. R. Mucciolo, N. M. R. Peres, and A. H. Castro Neto, Phys. Rev. B **83**, 165402 (2011).

[24] A. Ferreira, T. G. Rappoport, M. A. Cazalilla, and A. H. Castro Neto, Phys. Rev. Lett. **112**, 066601 (2014).

[25] L. Liu, C.-F. Pai, Y. Li, H. W. Tseng, D. C. Ralph, and R. A. Buhrman, Science **336**, 555 (2012); M. Morota, Y. Niimi, K. Ohnishi, D. H. Wei, T. Tanaka, H. Kontani, T. Kimura, and Y. Otani, Phys. Rev. B **83**, 174405 (2011).

[26] K. T. Chan, J. B. Neaton, and Marvin L. Cohen, Phys. Rev. B **77**, 235430 (2008).

[27] D. M. Duffy and J. A. Blackman, Phys. Rev. B **58**, 7443 (1998).

[28] T. Eelbo, M. Waśniowska, P. Thakur, M. Gyamfi, B. Sachs, T. O. Wehling, S. Forti, U. Starke, C. Tieg, A. I. Lichtenstein, and R. Wiesendanger, Phys. Rev. Lett. **110**, 136804 (2013).

[29] K. F. Kelly, E. T. Mickelson, R. H. Hauge, J. L. Margrave, and N. J. Halas, Proc. Natl. Acad. Sci. (USA) **97**, 10318 (2000); C Gómez-Navarro, J. C. Meyer, R. S. Sundaram, A. Chuvilin, S. Kurasch, M. Burghard, K. Kern, and U. Kaiser, Nano Lett. **10**, 1144 (2010).

[30] Z. H. Ni, L. A. Ponomarenko, R. R. Nair, R. Yang, S. Anissimova, I. V. Grigorieva, F. Schedin, P. Blake, Z. X. Shen, E. H. Hill, K. S. Novoselov, and A. K. Geim, Nano Lett. **10**, 3868 (2010).

[31] M. Jaiswal, C. Haley, Y. X. Lim, Q. Bao, C. T. Toh, K. P. Loh, and B. Özyilmaz, ACS Nano **5**, 888 (2011).

[32] J. H. Chen, W. G. Cullen, C. Jang, M. S. Fuhrer, and E. D. Williams, Phys. Rev. Lett. **102**, 236805 (2009).

[33] R. A. Horn and C. R. Johnson, *Topics in Matrix Analysis* (Cambridge University Press, Cambridge, 1991).

[34] G. W. Semenoff, Phys. Rev. Lett. **53**, 2449 (1984).

[35] C. L. Kane and E. J. Mele, Phys. Rev. Lett. **95**, 226801 (2005).

[36] T. Ando, T. Nakanishi, and M. Igami, J. Phys. Soc. Jpn. **68**, 3994 (1999).

[37] Y. A. Bychkov and E. I. Rashba, J. Phys. C **17**, 6039 (1984).

[38] E. McCann and V. I. Fal'ko, Phys. Rev. Lett. **108**, 166606 (2012).

[39] C. Bena and S. A. Kivelson, Phys. Rev. B **72**, 125432 (2005).

[40] B. A. Lippmann and J. Schwinger, Phys. Rev. **79**, 469 (1950).

[41] K. Výborný, A. A. Kovalev, J. Sinova, and T. Jungwirth, Phys. Rev. B **79**, 045427 (2009).

[42] T. Jungwirth, J. Wunderlich, and K. Olejnik, Nat. Mater. **11**, 382 (2012).

[43] D. A. Abanin, S. V. Morozov, L. A. Ponomarenko, R. V. Gorbachev, A. S. Mayorov, M. I. Katsnelson, K. Watanabe, T. Taniguchi, K. S. Novoselov, L. S. Levitov, and A. K. Geim, Science **332**, 328 (2011).

[44] B. Gu, I. Sugai, T. Ziman, G. Y. Guo, N. Nagaosa, T. Seki, K. Takanashi, and S. Maekawa, Phys. Rev. Lett. **105**, 216401 (2010).

[45] C. Brüne, A. Roth, E. G. Novik, M. König, H. Buhmann, E. M. Hankiewicz, W. Hanke, J. Sinova, and L. Molenkamp, Nat. Phys. **6**, 448 (2010).

[46] D. V. Fedorov, M. Gradhand, S. Ostanin, I. V. Maznichenko, A. Ernst, J. Fabian, and I. Mertig, Phys. Rev. Lett. **110**, 156602 (2013).

[47] N. Nagaosa, J. Sinova, S. Onoda, A. H. MacDonald, and N. P. Ong, Rev. Mod. Phys. **82**, 1539 (2010).

[48] D. A. Abanin, A. V. Shytov, and L. S. Levitov, Phys. Rev. Lett. **105**, 086802 (2010).

[49] V. V. Cheianov, O. Syljuasen, B. L. Altshuler, and V. Fal'ko, Phys. Rev. B **80**, 233409 (2009).

[50] V. V. Cheianov, O. Syljuasen, B. L. Altshuler, and V. I. Fal'ko, Europhys. Lett. **89**, 56003 (2010).

[51] S. Kopylov, V. Cheianov, B. L. Altshuler, and V. I. Fal'ko, Phys. Rev. B **83**, 201401 (2011).

[52] P. O. Löwdin, J. Chem. Phys. **19**, 1396 (1951).